Stress rotations and the long-term weakness of the Median Tectonic Line and the Rokko-Awaji Segment

Vincent Famin, Hugues Raimbourg, Sebastian Garcia, Nicolas Bellahsen, Yohei Hamada, Anne-Marie Boullier, Olivier Fabbri, Laurent Michon, Takahiko Uchide, Tullio Ricci, et al.

HAL Id: hal-01111609
https://hal.archives-ouvertes.fr/hal-01111609

Submitted on 13 Apr 2015

Stress rotations and the long-term weakness of the Median Tectonic Line and the Rokko-Awaji Segment

Vincent Famin[1], Hugues Raimbourg[2], Sebastian Garcia[3], Nicolas Bellahsen[4], Yohei Hamada[5], Anne-Marie Boullier[6], Olivier Fabbri[7], Laurent Michon[1], Takahiko Uchide[8], Tullio Ricci[9], Tetsuro Hirono[10], and Kuniyo Kawabata[11]

[1]Laboratoire Géosciences Réunion, Université de La Réunion, Institut de Physique du Globe de Paris, Sorbonne Paris Cité, UMR 7154 CNRS, Saint-Denis, France, [2]Institut des Sciences de la Terre d'Orléans, UMR CNRS 6113, Université d'Orléans, Orléans, France, [3]FR Geologie, Freie Universität Berlin, Berlin, Germany, [4]Institut des Sciences de la Terre de Paris, UMR CNRS 7193, Université Pierre et Marie Curie Paris 06, Paris, France, [5]Kochi Institute of Core Sample Research, Japan Agency for Marine-Earth Science and Technology, Kochi, Japan, [6]CNRS, ISTerre, Université Grenoble Alpes, Grenoble, France, [7]Laboratoire Chrono-Environnement, UMR CNRS 6249, Université de Franche-Comté, La Bouloie - UFR Sciences et Techniques, Besançon, France, [8]Geological Survey of Japan, National Institute of Advanced Industrial Science and Technology, Tukuma, Japan, [9]Instituto Nazionale di Geofisica e Vulcanologia, Rome, Italy, [10]Department of Earth and Space ScienceGraduate School of Science, Osaka University, Toyonaka, Japan, [11]Kagoshima University Museum, Kagoshima, Japan

Abstract We used a field analysis of rock deformation microstructures and mesostructures to reconstruct the long-term orientation of stresses around two major active fault systems in Japan, the Median Tectonic Line and the Rokko-Awaji Segment. Our study reveals that the dextral slip of the two fault systems, active since the Plio-Quaternary, was preceded by fault normal extension in the Miocene and sinistral wrenching in the Paleogene. The two fault systems deviated the regional stress field at the kilometer scale in their vicinity during each of the three tectonic regimes. The largest deviation, found in the Plio-Quaternary, is a more fault normal rotation of the maximum horizontal stress to an angle of 79° with the fault strands, suggesting an extremely low shear stress on the Median Tectonic Line and the Rokko-Awaji Segment. Possible causes of this long-term stress perturbation include a nearly total release of shear stress during earthquakes, a low static friction coefficient, or low elastic properties of the fault zones compared with the country rock. Independently of the preferred interpretation, the nearly fault normal orientation of the direction of maximum compression suggests that the mechanical properties of the fault zones are inadequate for the buildup of a pore fluid pressure sufficiently elevated to activate slip. The long-term weakness of the Median Tectonic Line and the Rokko-Awaji Segment may reside in low-friction/low-elasticity materials or dynamic weakening rather than in preearthquake fluid overpressures.

1. Introduction

The state of stress of major faults in the crust is intimately related to the concept of weak faults. According to laboratory measurements of rock friction coefficients ($0.6 < \mu < 0.85$) [*Byerlee,* 1978], faults should be oriented at a low angle ($<60°$) to the regional maximum principal stress in order to slip under hydrostatic pore pressure ($\sigma_1 \geq \sigma_2 \geq \sigma_3$ being the maximum, intermediate, and minimum principal stress, respectively). However, some faults like the San Andreas fault in California, the Malborough fault in New Zealand, or the Denali fault in Alaska must be weak ($\mu < 0.3$) because they slip at a high angle to σ_1 (60–90°) and hence at low resolved shear stress on the fault plane [*Balfour et al.,* 2005; *Hickman and Zoback*, 2004; *Mount and Suppe*, 1987; *Wesson and Boyd*, 2007; *Zoback et al.,* 1987]. Proposed explanations include low-friction fault materials [e.g., *Lockner et al.,* 2011], dynamic mechanisms of friction reduction during earthquakes [e.g., *Di Toro et al.,* 2004, and references therein], or elevated (i.e., greater than hydrostatic) pore fluid pressures in the fault zone before an earthquake [e.g., *Rice,* 1992]. In theory, each category of weakening processes should be associated with a specific pattern of stress orientations. For example, on faults at high angle with the regional direction of maximum compression like San Andreas, low-friction materials should correspond to an intrinsically low level of shear stress on the fault plane, and thus to σ_1 remaining at high angle with the fault. This is also true if fault weakness is due to dynamic mechanisms of friction reduction, with some temporal and spatial
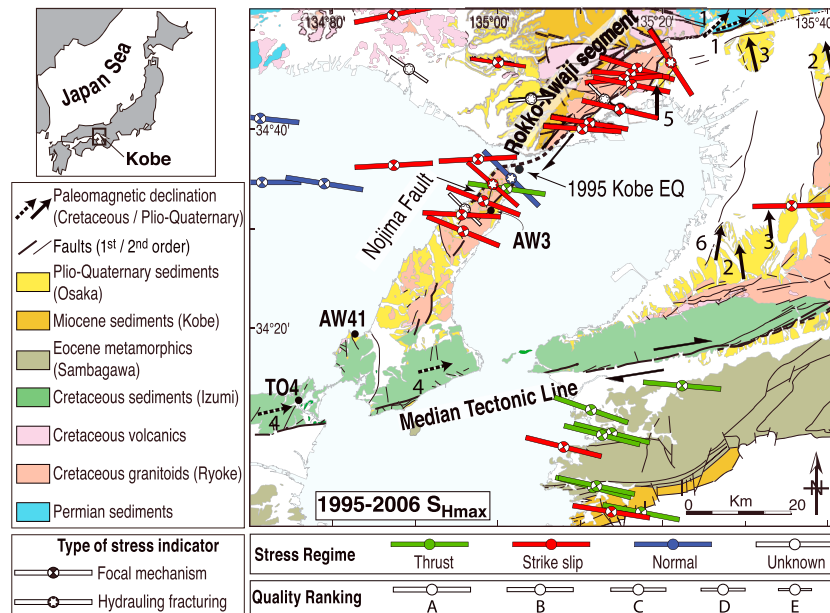
Figure 1. Geological map of the study area showing the directions of maximum horizontal stress (S_{Hmax}) during the 1992–2006 period, as inferred from earthquake focal mechanisms and hydraulic fracturing tests [*Dziewonski et al.,* 1996; *Ikeda et al.,* 2001; *Townend and Zoback,* 2006]. Also represented are paleomagnetic declination data (1, [*Uno,* 2002]; 2, [*Iwaki and Hayashida,* 2003]; 3, [*Hayashida et al.,* 1996]; 4, [*Kodama,* 1989]; 5, [*Hyodo et al.,* 2006]; 6, [*Maenaka,* 1979]) and the locations of three microtectonic sites illustrating data processing (AW41, AW3, and TO4).

variations of stress orientations depending on transient fault asperities. On the contrary, weak rupture by an increasing fluid overpressure should coincide with a reorientation of σ_1 to a more acute angle with the fault in its vicinity (lower than twice the optimum reactivation angle, i.e., about 60°), otherwise the fluid pressure necessary for slip would lead to tensile failure and the release of pressure [*Rice,* 1992; *Sibson,* 1985].

In practice, however, the pattern of stress perturbations around faults is a matter of vigorous debate. In some locations near San Andreas, the azimuth of σ_1 inversed from earthquake focal mechanisms seemed to rotate to more acute angles as approaching the fault, but this rotation has not been confirmed by larger earthquake catalogs [*Hardebeck and Hauksson,* 1999, 2001; *Hardebeck and Michael,* 2004; *Provost and Huston,* 2003; *Townend and Zoback,* 2004]. The problem is that focal mechanisms only offer a kilometer-scale spatial resolution, while it is likely that stress deviations occur at the meter scale in the damaged zone or in the core of faults [*Faulkner et al.,* 2006; *Healy,* 2008; *Tembe et al.,* 2009]. Borehole stress measurements may circumvent this problem [e.g., *Hickman and Zoback,* 2004], but they only constrain the stress state along the trajectory of drilling and thus do not help for the determination of along-strike variations of stresses. To date, scientific drilling across the San Andreas fault has not yet allowed a definitive discrimination of the most effective weakening mechanism [*Zoback et al.,* 2011], nor an answer about the existence or absence of prerupture elevated fluid pressures [*Wang,* 2011].

To improve our knowledge of the stress state of faults, another possibility is to study the deformation pattern around exhumed fault zones and to interpret this deformation in terms of stress orientations. Such methods allow the identification of spatial variations of deformation patterns, and possibly stress orientations, at the outcrop scale across and along strike of the faults [*Homberg et al.,* 1997, 2004], with the drawback that these variations are ill constrained in time. For our study, we targeted seismogenic faults that are, unlike the San Andreas fault, oriented at an angle ≤60° relative to the present-day regional direction of maximum compression. On such faults, weak minerals or dynamic weakening processes should induce a deflection of the maximum compression toward the fault normal direction, whereas abnormally elevated fluid pressures should not. The first case study is the Median Tectonic Line, the largest intraplate fault of Japan, which lies at an angle of 20–40° to the regional compression inferred from earthquake focal mechanisms (Figure 1) and has been geodetically locked over a ~30 year record [*Tabei et al.,* 2007]. The second example is the Rokko-Awaji

Segment (Figure 1), with particular attention being paid to the Nojima fault that ruptured in the 1995 Kobe earthquake (M_{JMA} = 7.2), killing 6400 persons. The Nojima fault, oriented at 45–65° to the regional compression, was also recognized as noncreeping prior to the Kobe earthquake [*Zhao and Takemoto*, 1998].

The two fault systems were initiated during the Cretaceous, cutting through Ryoke granitoids with a left lateral slip due to an arc oblique convergence [*Takagi*, 1986]. In Campanian to Maestrichtian times (75 to 65 Ma), the motion of the Median Tectonic Line opened a pull-apart basin filled with Izumi Group sediments [*Miyata*, 1990]. From purely left lateral, the slip of the Median Tectonic Line became transtensional in the Paleocene, exhuming the Sambagawa metamorphic belt [*Kubota and Takeshita*, 2008]. From the Paleocene to the Eocene (56 to 34 Ma), the Nojima fault appears to have slipped with a dextral movement [*Lin*, 2001; *Murakami and Tagami*, 2004; *Otsuki et al.,* 2003; *Zwingmann et al.,* 2010], whereas the activity of the other faults in the Rokko-Awaji Segment is unknown. In Eocene and Oligocene times (from 45 to 25 Ma), sinistral drag of the Median Tectonic Line folded the Izumi Group as a synclinal structure with an axis plunging 30° east [*Kodama*, 1986]. During the Miocene, the opening of the Japan Sea caused a NW-SE extension [*Fournier et al.,* 1995] and a ~40° clockwise rotation of Central and SW Japan [*Fournier et al.,* 1995; *Otofuji and Matsuda*, 1996], and formed the Kobe sedimentary basin (23 to 14 Ma). This extension reactivated the Median Tectonic Line as a normal fault [*Kubota and Takeshita*, 2008], whereas the Rokko-Awaji Segment seems to have experienced a period of quiescence during this period [*Boullier et al.,* 2004]. Since the middle Pliocene, no significant rotation has occurred in the study area (Figure 1), and the two fault systems have a dextral slip due to the NW-SE convergence of the Philippine Sea and Amuria plates, forming a depression filled with Osaka Group sediments (from 3 to 1 Ma).

The present-day structure of the Median Tectonic Line is made of a ~10 m thick fault gouge surrounded by mylonites, for a total half width of ~500 m [*Ikeda et al.,* 2013; *Maruyama and Lin*, 2004]. The Nojima fault, the best studied fault of the Rokko-Awaji Segment, is made of a 15–20 cm thick fault core, surrounded by a 5–20 m thick zone of foliated cataclasites, and a damaged zone of faulted Ryoke granitoids. The total half width of the Nojima fault zone has been estimated to 15–30 m according to borehole geophysics, drill core analyses, and outcrops near the drill sites [*Ito and Kiguchi*, 2005; *Lin et al.,* 2001; *Lockner et al.,* 2009], or to 75–150 m according to the analysis of trapped waves [*Mizuno and Nishigami*, 2006; *Mizuno et al.,* 2008]. Note, however, that unlike the Median Tectonic Line, the Rokko-Awaji Segment is a system of several faults parallel to each other, separated by up to 5 km, and thus the true width of deformed rocks around this system may be larger than the sum of the individual fault zones.

2. Methods

We analyzed deformation microstructures and mesostructures in the field to reconstruct the long-term orientation of stresses around the two faults. Deformation structures include small-scale striated faults (<2 m in length) or extension fractures (<10 cm) occasionally filled with syndeformation minerals (calcite ± quartz ± oxides), dikes, fold axes, and tilted beddings. For the Nojima area of the Rokko-Awaji Segment, the data set also includes published long-term stress orientation measurements from the analysis of microcracks [*Takeshita and Yagi*, 2001] and stress memory in core samples [*Yamamoto and Yabe*, 2001; *Yamamoto et al.,* 2002] but does not include the distribution of fractures deduced from borehole logging [*Ito and Kiguchi*, 2005] because the kinematics of these fractures is not known. Microstructures and mesostructures were measured at various distances of the faults from almost intact rocks (hereafter called the far field), to strongly deformed and altered rocks interpreted as the damaged zones, and even to the pseudotachylite bearing core zone of the Nojima fault [*Lin et al.,* 2001; *Ohtani et al.,* 2001; *Otsuki et al.,* 2003; *Tanaka et al.,* 2001, 2007]. A confidence level was attributed to the observed kinematics on each deformation marker (certain, probable, supposed, and unknown), using the convention of fault slip analysis [*Angelier*, 1984; *Delvaux and Sperner*, 2003; *Sperner et al.,* 2003]. Following the recommendations of *Sperner and Zweigel* [2010], the data were sorted manually into subsets, based on field-observed chronological relationships or geometrical reasoning (e.g., rotation of one principal stress axis to the vertical by restoration of the bedding stratification to the horizontal, [*Lacombe,* 2012]).

Stress orientations were obtained by inversion of fault slip data and extension fractures, or deduced from the average orientation of the other strain markers. Stress inversion of brittle deformation markers is based on

Table 1. Threshold Values of Parameters Used in the Determination of Stress Tensor Quality According to the Ranking Scheme of the World Stress Map Project [*Sperner et al.,* 2003] and to the Stress Inversion Procedure of *Delvaux and Sperner* [2003][a]

Tensor Quality, QR_W	Number of Data, n	Percentage of Data, n/n_t	Average Confidence Level of Data, CL_W	Averag Slip Deviation, α_W	Average Data Type, DT_W
A	≥ 25	≥ 60	≥ 0.70	≤ 9	≥ 0.90
B	≥ 15	≥ 45	≥ 0.55	≤ 12	≥ 0.75
C	≥ 10	≥ 30	≥ 0.40	≤ 15	≥ 0.50
D	≥ 6	≥ 15	≥ 0.25	≤ 18	≥ 0.25
E	$4 < n < 6$	< 15	< 0.25	> 18	< 0.25

[a]Tensors with $CL_W < 0.40$, $\alpha_W > 15°$, or $DT_W < 50$ were not considered for paleostress reconstruction.

the following assumptions: (1) the rock behaves as a linear elastic material around the deformation microstructures, i.e., stress and strain are coaxial according to Hooke's law; (2) displacements on fractures are small compared to the representative element volume of the rock mass; (3) the fractures do not interact with each other; (4) for faults, the slip vector on each fault plane, indicated by slickensides, is collinear to the maximum shear stress on this fault plane [*Bott,* 1959; *Wallace,* 1951]. Some authors argued that the first hypothesis is not always verified [e.g., *Twiss and Unruh,* 1998]. In practice, however, several comparisons provided ample evidence that the stress orientations obtained by inversion of brittle deformation structures and other methods (earthquake focal mechanisms, boreholes, or stress relief techniques) are in good agreement [*Lacombe,* 2012; *Sperner et al.,* 2003].

Stress inversions were performed using the Win_Tensor program [*Delvaux,* 2013]. The inversion procedure used by this program, described in detail in *Delvaux and Sperner* [2003] and employed in many published applications [e.g., *Delvaux et al.,* 2012; *Kipata et al.,* 2013] is only briefly recalled here. The inversion of fractures allows reconstructing a reduced tectonic stress tensor composed of four parameters, the three orthogonal directions of principal stresses and the ratio $R = (\sigma_2 - \sigma_3)/(\sigma_1 - \sigma_3)$. The inversion proceeds by iterations to find the best fit reduced stress tensor that minimizes the slip deviation (the average angle between the computed and measured slip vectors), maximizes the shear stress magnitude, and minimizes the normal stress magnitude on faults (to favor slip), while minimizing the shear stress and normal stress magnitudes on extension fractures (to impede slip and favor opening). The horizontal maximum and minimum stress orientations (S_{Hmax} and S_{hmin}, respectively) and their 1σ standard deviation are computed from the values and uncertainties of the four parameters of the reduced stress tensor using the method of *Lund and Townend* [2007].

The quality of each reduced stress tensor was estimated using two indexes, both ranging from A (best) to E (worst). The first index, QR_W, rates the quality of principal stress orientations using the ranking scheme of the World Stress Map Project [*Sperner et al.,* 2003]. QR_W is determined by threshold values (recalled in Table 1) of the following criteria: (1) the number of data per tensor n, (2) the proportion of data used in the tensor relative to the total number of data measured at each outcrop n/n_t, (3) the average slip deviation α_W, (4) the average confidence level of the subset of deformation markers CL_W, and (5) the average type of data used for tensor determination DT_W, based on the usefulness of each deformation marker in stress inversion (1 for striated faults; 0.5 for tension fractures or dikes, and 0.25 for faults with slip sense but no striation). QR_W is defined by the lowest of these criteria, and thus not only by the standard deviation around the computed orientations. The second index, QR_T, rates the quality of R estimates using all the criteria of QR_W, plus two criteria related to the diversity of fault planes. Tensors with $CL_W < 0.40$, $\alpha_W > 15°$ or $DT_W < 0.50$ were not retained and the corresponding data were considered as unexplained. Because the reduced stress tensors are obtained by inversion of brittle deformation microstructures accumulated over a geological time (as opposed to tensors obtained by inversion of earthquakes), they are hereafter called "paleostresses." Given the maximum burial of Ryoke, Izumi, Kobe, and Osaka rocks (3.5, 5, 1, and 0.5 km, respectively), these paleostresses pertain to the upper 5 km of the crust.

3. Results

The separation of the data into subsets, the determination of paleostress solutions and their chronological interpretation are illustrated with three examples (Figures 2–4). The first example is the site AW41 in
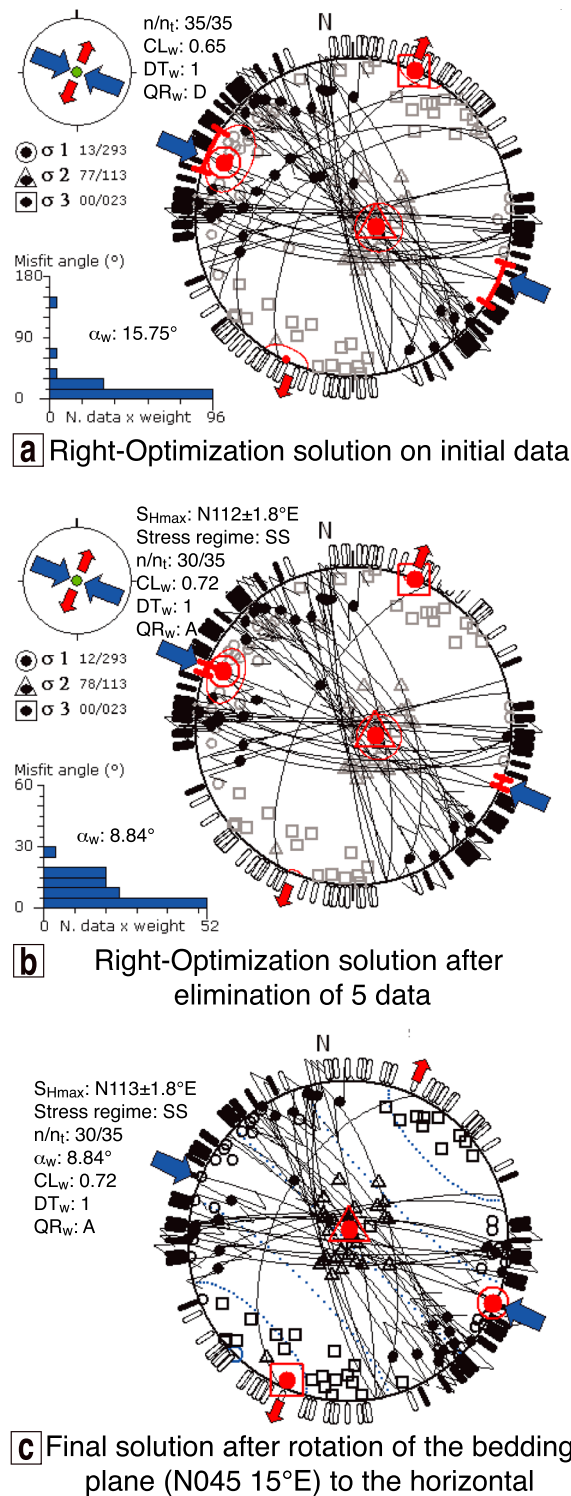
a Right-Optimization solution on initial data

b   Right-Optimization solution after
            elimination of 5 data

c Final solution after rotation of the bedding
     plane (N045 15°E) to the horizontal

Figure 2. Example of data processing for a measurement site (AW41) in Plio-Quaternary sediments of the Osaka Group (a) before and (b) after rejection of non-compatible data (see Figure 1 for site location). (c) Paleostress tensor solution after correction of the tilt of the bedding stratification. SS means strike-slip stress regime (σ_1, σ_3 horizontal). See text and Table 1 for the definition of other symbols.

Plio-Quaternary sediments of the Osaka Group (Figure 2, see Figure 1 for location). Running the inversion method on the entire set of fault slip data collected at this site ($n_t = 35$) yields a strike-slip paleostress solution. The quality of the reduced tensor is nevertheless quite low ($QR_w = $ D; Figure 2a), because of a few mechanically incompatible faults (e.g., with opposed slip senses) in the data set, implying a high slip deviation ($\alpha_w = 15.75°$). We eliminated these data to reduce the slip deviation, keeping in mind that rejecting data also reduces n and n/n_t, which may alter QR_w and QR_T. The rejection of five data improves the slip deviation ($\alpha_w = 8.84°$) and the quality of stress orientation estimates ($QR_w = $ A; Figure 2b). This tensor corresponds to a strike-slip paleostress regime with S_{Hmax} oriented N112 $\pm$ 1.8°E, obviously younger than the deposition of the Osaka Group sediments at this site (i.e., younger than 2 Ma; Table 2). The rejected data do not constitute a tensor and are thus considered as unexplained. Given the moderate dip of the bedding stratification (15° toward the NW), it is possible that the Osaka sediments, and the faults in them, underwent a slight tilt after their formation. However, the paleostress regime and the orientation of S_{Hmax} remain nearly unchanged (N113 $\pm$ 1.8°E) after the restoration of the bedding plane to the horizontal (Figure 2c), showing that effect of this rotation is negligible.

The second example is the site AW3 near the Kushumoto fault (another fault of the Rokko-Awaji Segment), at the contact between middle Miocene sediments of the Kobe Group and the Ryoke granitic basement (Figure 3, see Figure 1 for location). This outcrop displays meter-scale normal faults cutting the basement and the lower strata of the sedimentary unit, and sealed by the undeformed upper strata (Figure 3a). Inversion of the entire data set of normal faults ($n_t = 15$) yields an extensional paleostress regime. As in the previous example, the reduced tensor is of low quality, because it incorporates mechanically incompatible faults ($\alpha_w = 25.13°$, $QR_w = $ E; Figure 3b). After removing the three fault slip data having the highest misfit angle relative to the resolved shear stress, the final optimal solution is a normal faulting regime with S_{hmin} at N108 $\pm$ 28°E ($\alpha_w = 9.2°$, $QR_w = $ C; Figure 3c). According to the sealing of the faults by sediments, this synsedimentary
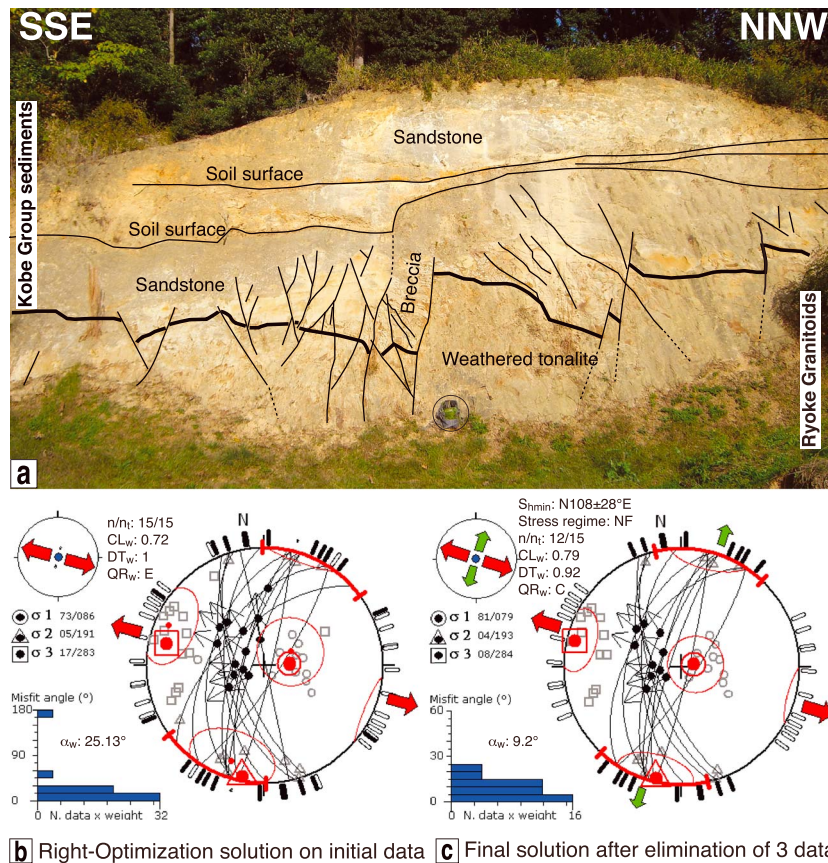
Figure 3. Example of data processing for a measurement site (AW3) in Miocene sediments of the Kobe Group (see Figure 1a for site location). (a) Outcrop showing the normal faults cutting through the tonalite basement of the Ryoke Group and the lower strata of the Kobe Group sediments, and covered by undeformed upper strata. Paleostress tensor solutions (b) before and (c) after rejection of the noncompatible data. Faults represented without striation have an observed component of normal slip. NF means normal faulting (σ_2, σ_3 horizontal). See text and Table 1 for the definition of other symbols.

extension occurred between the beginning and the end of the deposition of the Kobe Group at this site, i.e., between 18 and 14 Ma (Table 2).

The third example is the site TO4 near the Median Tectonic Line, taken in folded sediments of the late Cretaceous Izumi Group (Figure 4, see Figure 1 for location). The entire set of faults ($n_t = 52$; Figure 4a) contains two subsets of incompatible faults. The first subset is made of strike-slip faults with NE or SW trending slickensides (Figure 4b) and the second subset of faults with NW trending slickensides (Figure 4c). In the field, some faults have been observed containing the two populations of slickensides, the NW trending population cutting the NE of SW trending one. This suggests that the second set contains reactivated faults of the first set and therefore postdates it. Inversion of the first subset ($n = 27$) yields a good reduced tensor ($\alpha_w = 11.56°$, $QR_w = B$; Figure 4b) with a horizontal σ_1 axis and oblique σ_2 and σ_3 axes. The second subset ($n = 18$) also yields an acceptable tensor ($\alpha_w = 26°$; $QR_w = C$; Figure 4c) with oblique σ_1 and σ_2 axes and a horizontal σ_3 axis. Seven data have been rejected because they are noncompatible with either of the two subsets or because they decrease the quality of the tensors. The bedding stratification being strongly tilted, it is possible that any of the two subsets has been affected by the folding of the Izumi Group. To test this eventuality, we corrected the reduced stress tensors of the bedding tilt, first with a restoration of the Izumi synclinal axis to the horizontal (i.e., a 30°W rotation around a N-S axis [*Kodama*, 1989]), and then with a rotation of the strata (N059 33°S) toward the horizontal. Applying this correction to the first subset restores the faults into the attitude of subvertical neoformed strike-slip faults and sets upright the two oblique principal stress axes of the tensor (Figure 4c). This correction is supported by the fact that one principal stress
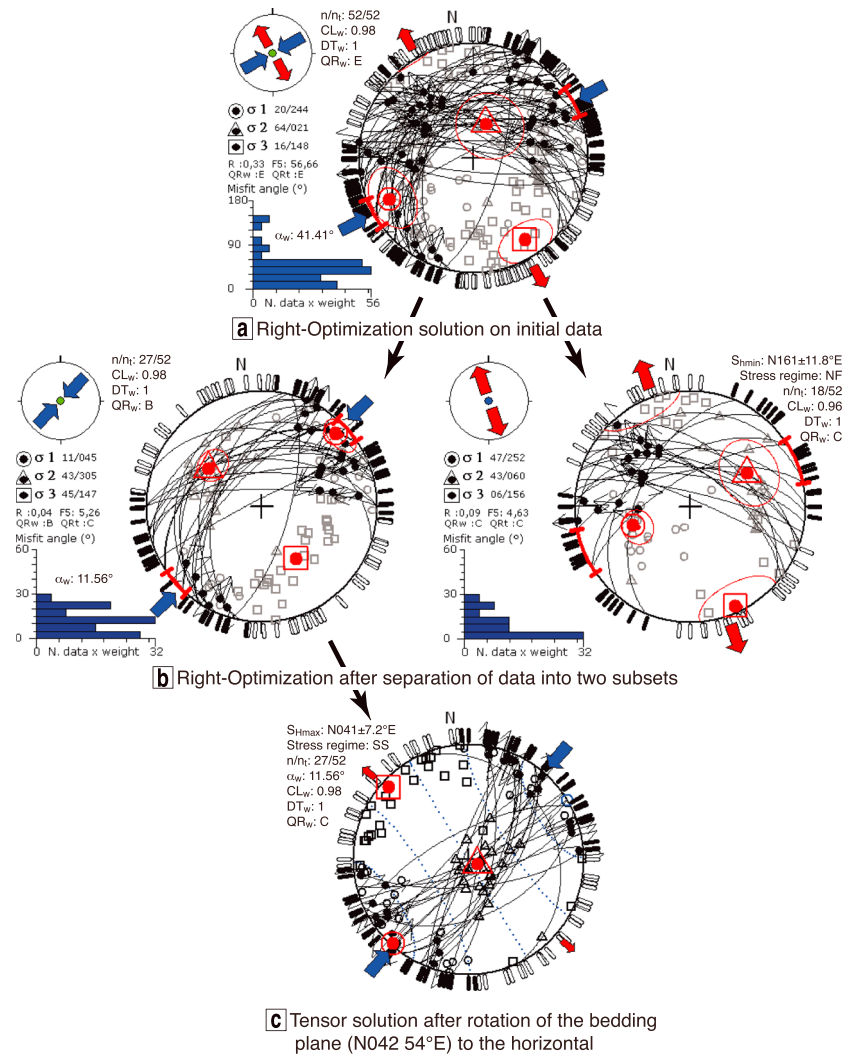
a Right-Optimization solution on initial data

b Right-Optimization after separation of data into two subsets

c Tensor solution after rotation of the bedding plane (N042 54°E) to the horizontal

Figure 4. Example of data processing for a measurement site (TO4) in Campanian-Maastrichtian sediments of the Izumi Group (see Figure 1 for site location). (a) Initial data set. (b) Separation of the data into two subsets sorted by mechanical compatibility and field observations. Seven data are rejected in this process. (c) Reduced stress tensor of the first subset after correction of the Izumi Group folding. SS means strike-slip (σ_1, σ_3 horizontal), NF normal faulting (σ_2, σ_3 horizontal). See text and Table 1 for the definition of other symbols.

axis is often vertical in nature [*Lacombe*, 2012]. We therefore interpret this first tensor as being due to a strike-slip paleostress regime with S_{Hmax} oriented N049 ± 7.2°, younger than the Izumi group (65 Ma) but older than its folding (initiated at 45 Ma). On the other hand, the same correction applied to the second set yields neither a plausible attitude of the faults nor an upright position of the tensor principal stress axes. Consequently, we interpret the second tensor as due to an extensional paleostress regime with S_{hmin} oriented N161 ± 11.8°E, which reactivated the strike-slip faults of the first subset after the folding of the Izumi Group ended up at 25 Ma.

The same analysis applied to the entire data set reveals that 88% of the deformation structures (i.e., 989 out of 1119 data) may be explained by three phases of fault activity (Figures 5 and 6, Table 2, full data set available in the supporting information). The first, youngest paleostress regime, found in all rocks and hence younger than 2 Ma, is a strike-slip faulting with S_{Hmax} oriented N160 – 170°E near the Median Tectonic Line to N110 − 120°E near the Rokko-Awaji Segment (Figure 5a), consistent with a right lateral movement of the two fault systems. The second paleostress regime, found in rocks older than the Osaka sediments (i.e., after 18 Ma and before 3 Ma), is an extension with S_{hmin} oriented N170 − 180°E near the Median Tectonic Line and

Table 2. Summary of Tensor Types, Paleostress Orientations, and Chronological Criteria Between the Obtained Tensors

Site Name [a]	Stratigraphy [a]	Age (Ma) [a]	Distance From Fault (m)	Left Lateral Tectonic Regime [b]	Stress Regime [b]	Azimuth of S_{Hmax} ± 1 SD (°E)	Q_{RW} [c]	R ± 1 SD [d]	Q_{RT} [c]	Extensional Tectonic Regime [b]	Stress Regime [b]	Azimuth of S_{hmin} ± 1 SD (°E)	Q_{RW} [c]	R ± 1 SD [d]	Q_{RT} [c]	Right Lateral Tectonic Regime [b]	Stress Regime [b]	Azimuth of S_{Hmax} ± 1 SD (°E)	Q_{RW} [c]	R ± 1 SD [d]	Q_{RT} [c]
Wakayama Area																					
WA1	Izumi Group	72 – 65	1360	Pretilt	SS	49 ± 11	C	0.25 ± 0.3	C	Post-tilt	NF	174 ± 16.5	B	0.47 ± 0.22	B	Post-tilt and post-extension tensor	SS	168 ± 8.9	C	0.79 ± 0.36	C
WA3	Izumi Group	72 – 65	1210	Pretilt	TF	124 ± 15	D	-	-	Post-tilt and anterior to fold axis rotation	NF	9 ± 12.4	B	0.15 ± 0.11	-	Post-tilt and post-extension tensor	SS	73 ± 11.1	B	0.39 ± 0.21	B
WA4	Izumi Group	72 – 65	2510	Syntilt	NF	18 ± 27.4	C	0.27 ± 0.15	C	-	-	-	-	-	-	-	-	-	-	-	-	-
WA5	Izumi Group	72 – 65	1650	Pretilt	SS	59 ± 7.8	B	0.36 ± 0.27	B	-	-	-	-	-	B	Post-tilt and post-LL tensor	SS	166 ± 3.2	D	0.06 ± 0.11	D
WA5	Izumi Group	72 – 65	1650	Pretilt	SS	20 ± 10.5	C	0.17 ± 0.12	C	-	-	-	-	-	-	-	-	-	-	-	-	-
WA5	Izumi Group	72 – 65	1650	Posttilt	SS	34 ± 6.9	B	0.31 ± 0.22	B	-	-	-	-	-	B	-	-	-	-	-	-	-
WA7	Izumi Group	72 – 65	730	Pretilt to syntilt, consistent with RL strike slip	UF	162 ± 15	C	-	-	Post-tilt	NF	161 ± 31.3	D	0.11 ± 0.07	-	-	-	-	-	-	D
Tokushima Area																					
WA8	Izumi Group	72 – 65	6850	Syntilt	SS	19 ± 11.8	C	0.28 ± 0.15	D	-	-	-	-	-	-	Post-tilt	SS	128 ± 7.7	C	0.08 ± 0.4	C
TO1	Izumi Group	72 – 65	230	Pretilt	SS	51 ± 8.7	B	0.02 ± 0.02	C	-	-	-	-	-	-	-	-	-	-	-	-
TO2	Izumi Group	72 – 65	8160	Pretilt	SS	43 ± 12.5	D	0.27 ± 0.1	D	Post-tilt	NF	172 ± 7.4	C	0.21 ± 0.14	D	-	-	-	-	-	D
TO3	Izumi Group	72 – 65	5580	Post-tilt	SS	65 ± 6.2	C	0.36 ± 0.36	C	-	-	-	-	-	C	-	-	-	-	-	-
TO4	Izumi Group	72 – 65	3360	Pretilt	SS	41 ± 7.2	B	0.04 ± 0.12	B	Post-tilt	NF	161 ± 11.8	C	0.1 ± 0.09	C	-	-	-	C	-	-
TO5	Izumi Group	83 – 65	7100	Pretilt or post-tilt	SS	33 ± 16.4	D	0.39 ± 0.21	E	Post-tilt and post-LL tensor	NF	169 ± 24.9	B	0.57 ± 0.17	B	Post-tilt. No criteria between extension and RL	SS	160 ± 3.7	D	0.72 ± 0.29	D
TO6-8	Izumi Group	72 – 65	750	-	-	-	-	-	-	Post-tilt	NF	116 ± 11.9	C	0.66 ± 0.28	-	Post-tilt and post-extension tensor	SS	173 ± 7.6	C	0.26 ± 0.24	C
TO9	Izumi Group	72 – 65	200	Pretilt or post-tilt	SS	50 ± 9.5	D	0.58 ± 0.19	D	-	-	-	-	-	-	Post-tilt and post-TF tensor	SS	174 ± 8	C	0.11 ± 0.22	C
Awaji Island																					
GSJ	Nojima Granodiorite	90 – 70	0	Posterior to Late Cretaceous	SS	130 ± 8.6	C	0.52 ± 0.21	C	Post-LL tensor and contains Miocene andesite dykes	NF	115 ± 16.4	C	0.45 ± 0.2	C	Post-LL tensor	NF	99 ± 19.7	D	0.14 ± 0.1	D
GSJ	Nojima core zone	56 ± 4	0	Core microstructures consistent with RL slip of the Nojima fault	SS	127 ± 9.7	C	-	-	-	-	-	-	-	-	-	-	-	-	-	-
DPRI	Nojima Granodiorite	90 – 70	330	Older than 56 ± 4 Ma	TF	146 ± 14.2	B	0.44 ± 0.19	B	Contains Miocene andesite dykes	NF	61 ± 17.5	C	0.18 ± 0.09	C	-	-	-	-	-	-
DPRI		90 – 70	330		SS	160	C	-	-	-	-	-	-	-	-	-	-	-	-	-	-

Table 2. (continued)

Site Name[a]	Stratigraphy[a]	Age (Ma)[a]	Distance From Fault (m)	Left Lateral — Tectonic Regime[b]	LL Stress Regime[b]	LL Azimuth of S_{Hmax} ± 1 SD (°E)	LL QR_W[c]	LL R ± 1 SD[d]	LL QR_T[c]	Extensional — Tectonic Regime[b]	Ext Stress Regime[b]	Ext Azimuth of S_{hmin} ± 1 SD (°E)	Ext QR_W[c]	Ext R ± 1 SD[d]	Ext QR_T[c]	Right Lateral — Tectonic Regime[b]	RL Stress Regime[b]	RL Azimuth of S_{Hmax} ± 1 SD (°E)	RL QR_W[c]	RL R ± 1 SD[d]	RL QR_T[c]
	Nojima Granodiorite			Late Cretaceous [Takeshita and Yagi, 2001]	-	-	-	-	-	-	-	-	-	-	-	-	-	-	-	-	-
DPRI	Nojima Granodiorite	90 – 70	80	-	-	-	-	-	-	-	-	-	-	-	-	Plio-IV to present [Yamamoto and Yabe, 2001]	SS	113	C	-	-
DPRI	Nojima Granodiorite	90 – 70	25	-	-	-	-	-	-	-	-	-	-	-	-	Plio-IV to present [Yamamoto and Yabe, 2001]	SS	139	C	-	-
IKH	Nojima Granodiorite	96 – 65	930	-	-	-	-	-	-	-	-	-	-	-	-	Plio-IV to present [Yamamoto and Yabe, 2001]	SS	74	C	-	-
AW2	Shizuki tonalite	95 – 65	120	-	-	-	-	-	-	No chronological criteria	NF	137 ± 12.5	C	0.08 ± 0.07	-	-	-	-	-	-	-
AW17	Tsushigawa Granite	95 – 65	6500	Posterior to Late Cretaceous	SS	156 ± 11.4	C	0.4 ± 0.26	C	No chronological criteria between LL and extension	NF	98 ± 24.1	C	0.16 ± 0.1	C	-	-	-	-	-	-
AW21	Shizuki Tonalite	95 – 65	600	Posterior to Late Cretaceous	SS	141 ± 15.8	E	0.39 ± 0.31	E	-	-	-	-	-	-	-	-	-	-	-	-
AW23	Izumi Group	72 – 65	5600	-	-	-	-	-	-	Post-tilt	NF	156 ± 23.8	D	0.51 ± 0.3	D	Post-tilt and post-extension tensor	SS	124 ± 12.6	D	0.84 ± 0.2	D
AW27	Izumi Group	72 – 65	4000	-	-	-	-	-	-	Post-tilt	NF	170 ± 13.8	C	0.15 ± 0.1	C	-	-	-	-	-	-
AW37	Izumi Group	72 – 65	3400	Pretilt	SS	156 ± 19.5	D	0.46 ± 0.22	D	Post-tilt	NF	153 ± 11.3	D	0.37 ± 0.22	D	Post-tilt	NF	154 ± 6.1	E	0.49	E
AW40	Izumi Group	72 – 65	6430	Post-tilt	TF	32 ± 17.6	B	0.6 ± 0.15	D	-	-	-	-	-	-	Post-tilt and post-LL tensors	SS	147 ± 7.5	B	0.38 ± 0.31	C
AW40	Izumi Group	72 – 65	6430	Post-tilt	SS	36 ± 7.7	D	0.17 ± 0.12	D	-	-	-	-	-	-	-	-	-	-	-	-
AW45	Izumi Group	72 – 65	8100	Pretilt	SS	129 ± 5.1	D	0.63 ± 0.23	-	-	-	-	-	-	-	Post-tilt	SS	169 ± 13.9	B	0.29 ± 0.32	B
AW46	Izumi Group	72 – 65	4500	Pretilt	SS	113 ± 8.6	C	0.12 ± 0.08	C	-	-	-	-	-	-	-	-	-	-	-	-
AW51	Izumi Group	72 – 65	2200	-	-	-	-	-	-	Post-tilt, no chronology between thrust and extension tensors	NF	5 ± 23.3	C	0.33 ± 0.14	C	Post-tilt, no chronology between thrust and extension tensors	TF	166 ± 36.8	C	0.94 ± 0.08	C
AW52	Izumi Group	72 – 65	2340	-	-	-	-	-	-	Post-tilt	NF	3 ± 9.2	D	0.88 ± 0.16	D	-	-	-	-	-	-
AW53	Izumi Group	72 – 65	150	-	-	-	-	-	-	Post-tilt	NF	169 ± 17.9	E	0.35 ± 0.12	E	-	-	-	-	-	-
AW54	Izumi Group	72 – 65	370	Pretilt	SS	161 ± 24.6	D	0.26 ± 0.32	D	Post-tilt	NF	154 ± 13.4	B	0.64 ± 0.19	B	-	-	-	-	-	-
J1	Kobe Group	2	390	-	-	-	-	-	-	Post-sedimentation	NF	129 ± 26	C	0.2 ± 0.11	D	No criteria between NF and SS tensors	SS	125 ± 7	D	0.98 ± 0.23	E
AW1	Kobe Group	18 – 14	100	-	-	-	-	-	-	Post-sedimentation	NF	133 ± 8.8	C	0.67 ± 0.53	E	-	-	-	-	-	-
AW3	Contact Shizuki/Kobe	18 – 14	70	-	-	-	-	-	-	Synsedimentary in Kobe Group	NF	108 ± 28.7	C	0.13 ± 0.12	E	-	-	-	-	-	-
AW5	Kobe Group	18 – 14	1350	-	-	-	-	-	-	-	NF	147 ± 29.1	D	0.25 ± 0.15	E	-	UF	112 ± 15.8	E	0.39 ± 0.5	E

Table 2. (continued)

Site Name[a]	Stratigraphy[a]	Age (Ma)[a]	Distance From Fault (m)	Left Lateral						Extensional						Right Lateral					
				Tectonic Regime[b]	Stress Regime[b]	Azimuth of $S_{Hmax} \pm 1$ SD (°E)	QRw[c]	R ± 1 SD[d]	QRT[c]	Tectonic Regime[b]	Stress Regime[b]	Azimuth of $S_{hmin} \pm 1$ SD (°E)	QRw[c]	R ± 1 SD[d]	QRT[c]	Tectonic Regime[b]	Stress Regime[b]	Azimuth of $S_{Hmax} \pm 1$ SD (°E)	QRw[c]	R ± 1 SD[d]	QRT[c]
AW6	Contact Nojima/Kobe	18 – 14	1410	-	-	-	-	-	-	Post-sedimentation	-	-	-	-	-	No criteria between the two tensors	-	-	-	-	-
AW8	Kobe Group	18 – 14	380	-	-	-	-	-	-	Post-sedimentation	NF	146 ± 18.3	C	0.53 ± 0.27	C	Post-sedimentation	SS	112 ± 8.5	C	0.46 ± 0.46	E
AW10	Kobe Group	18 – 14	880	-	-	-	-	-	-	Post-sedimentation	NF	118 ± 23.7	D	0.5 ± 0.39	D	Post-sedimentation	UF	128 ± 11.6	D	-	-
AW9	Osaka Group	2 – 1	890	-	-	-	-	-	-	-	-	-	-	-	-	No criteria between the two tensors	-	-	-	-	-
AW11	Osaka Group	2 – 1	360	-	-	-	-	-	-	-	-	-	-	-	-	Pretilt to syntilt thrust	TF	113 ± 8	C	0.11 ± 0.23	D
AW16	Osaka Group	2	5100	-	-	-	-	-	-	-	-	-	-	-	-	Synsedimentation and/or post-sedimentation thrust	TF	138 ± 36.3	C	0.43 ± 0.21	E
AW41	Osaka Group	2	9500	-	-	-	-	-	-	-	-	-	-	-	-	Post-sedimentation	UF	108 ± 12.1	D	-	-
AW42	Osaka Group	2	250	-	-	-	-	-	-	-	-	-	-	-	-	Pretilt	SS	113 ± 1.8	A	0.08 ± 0.3	B
AW47	Osaka Group	2 – 1	6800	-	-	-	-	-	-	-	-	-	-	-	-	Post-tilt thrust	TF	113 ± 19.1	C	0.61 ± 0.21	C
AW47	Osaka Group	2 – 1	6800	-	-	-	-	-	-	-	-	-	-	-	-	Post-tilt	SS	105 ± 4.8	B	0.02 ± 0.11	C
AW49	Osaka Group	2	6500	-	-	-	-	-	-	-	-	-	-	-	-	Post-sedimentation and Pretilt extension	NF	111 ± 17.2	C	0.06 ± 0.05	C
AW49	Osaka Group			-	-	-	-	-	-	-	-	-	-	-	-	Post-sedimentation extension	NS	109 ± 13.1	C	0.44 ± 0.22	C
Osaka-Himeji Area																					
OS6	Arima Rhyolite	95 – 65	6750	-	-	-	-	-	-	Post-tilt	NF	111 ± 24.3	D	0.41	E	-	-	-	-	-	-
OS1	Kobe Group	23 – 14	3000	-	-	-	-	-	-	Post-sedimentation	NF	100 ± 27.6	C	0.1 ± 0.12	C	-	-	-	-	-	-
OS2-3	Rokko Granite + Kobe	18 – 14	3900	-	-	-	-	-	-	Post-sedimentation of Kobe Group	NF	135 ± 6.7	C	0.5 ± 0.17	D	Post-extension tensor	SS	151 ± 10.9	C	0.55 ± 0.21	C
OS4	Kobe Group	23 – 14	590	-	-	-	-	-	-	Post-sedimentation and ante tilt	NF	127 ± 12.9	D	0.53 ± 0.29	D	-	-	-	-	-	-
OS5	Contact Rokko/terrace	1 – 0.5	0	-	-	-	-	-	-	-	-	-	-	-	-	Synterrace sedimentation [Maruyama and Lin, 2004]	SS	135	D	-	-
OS7	Kobe Group	23 – 14	7100	-	-	-	-	-	-	Post-tilt	NF	157 ± 15.8	D	0.69 ± 0.22	E	-	-	-	-	-	-

Table 2. (continued)

Site Name[a]	Stratigraphy[a]	Age (Ma)[a]	Left Lateral Distance From Fault (m)	Tectonic Regime[b]	Stress Regime[b]	Azimuth of S_{Hmax} ± 1 SD (°E)	QR_W[c]	R ± 1 SD[d]	QR_T[c]	Extensional Tectonic Regime[b]	Stress Regime[b]	Azimuth of S_{hmin} ± 1 SD (°E)	QR_W[c]	R ± 1 SD[d]	QR_T[c]	Right Lateral Tectonic Regime[b]	Stress Regime[b]	Azimuth of S_{Hmax} ± 1 SD (°E)	QR_W[c]	R ± 1 SD[d]	QR_T[c]
Summary			Twenty-six tensors found in ante-Miocene rocks, 21 of which are strike-slips. Twenty-one tensors are consistent with left lateral strike slip on the Median Tectonic Line and the Rokko-Awaji Segment. Sixteen tensors have age constraints older than 45 Ma. Five tensors are post-tilt, and three have no chronological constraints. The timing of left lateral slip is therefore comprised between 65 and 25 Ma, and more likely between 65 and 45 Ma.							Twenty-nine extensional tensors found in ante-Pliocene rocks. Extensional tensors are post-tilt in Maestrichtian sediments, and syndeposition to post-deposition of Middle Miocene sediments. The timing of extension is therefore comprised between 23 and 3 Ma on the Median Tectonic Line and 18 and 3 Ma on the Rokko-Awaji Segment.						Thirty tensors found in all rocks, 19 of them are strike slip. All the tensors are consistent with right lateral movement on the Median Tectonic line and the Rokko-Awaji Segment. Ten tensors are posterior to the extension tensors, and eight occur in Plio-Quaternary sediments. Right lateral tensors are post-tilt in rocks older than Pliocene, and syntilt to post-tilt in Plio-Quaternary rocks. The timing of right lateral movement is therefore comprised between 2 and 0 Ma.					

[a]Site locations are provided in the supporting information. The stratigraphy and age interval of the geological units are taken from the geological maps of the study area [*Igi and Chosajo*, 1981; *Kawada et al.*, 1986; *Kurimoto and Komazawa*, 1998; *Makimoto et al.*, 1995].
[b]The stress regime refers to the faulting type and orientation of principal stresses: SS means strike-slip (σ_1, σ_3 horizontal; LL and RL for left lateral and right lateral, respectively), NF normal faulting (σ_2, σ_3 horizontal), TF thrust faulting (σ_1, σ_2 horizontal), and UF unknown faulting type (only one known principal stress axis).
[c]QR_W and QR_T refer to the quality rating systems of the World Stress Map project [*Sperner et al.*, 2003] and of *Delvaux and Sperner* [2003], respectively.
[d]$R = (\sigma_2 − \sigma_3)/(\sigma_1 − \sigma_3)$.

N130 − 140°E near the Rokko-Awaji Segment (Figure 5b). The Rokko-Awaji Segment, of previously unknown activity during the Miocene, was thus in fact reactivated as a normal fault system by the opening of the Japan Sea, as was the Median Tectonic Line during the same period [*Kubota and Takeshita*, 2008]. The third, oldest paleostress regime, found only in pre-Miocene rocks (i.e., after 65 Ma and before 23 Ma), is a strike-slip faulting with S_{Hmax} oriented N20 − 50°E near the Median Tectonic Line to N140 − 150°E near the Rokko-Awaji Segment (Figure 5c), consistent with a left lateral movement of the two fault systems. Our paleostress regimes are consistent in terms of orientation and age with the tectonic history of the two fault systems and the geodynamics of the region (Figure 6).

4. Discussion

4.1. Significance of Paleostresses

The first question to address is whether the spatial organization of deformation structures represents true deviations of the regional stress fields by the two fault systems. Around the San Andreas Fault, the direction of maximum shortening measured from fault slip data, recent fold axes, borehole breakouts, earthquake focal mechanisms, and shear wave splitting are in good agreement, which suggests that independent methods of stress determination from strain data yields comparable results near a major fault, provided that no rotation occurred [*Boness and Zoback*, 2006; *Miller*, 1998; *Mount and Suppe*, 1987; *Tavarnelli and Holdsworth*, 1999; *Townend and Zoback*, 2001, 2004]. According to the paleomagnetic record (Figure 1), there is no tectonic rotation in the study area since the Plio-Quaternary, and Southwest Japan moved as a rigid block from the Paleogene to the present. This suggests that deformation structures, and thus paleostress orientations, have not been modified relative to each other by tectonic rotations around a vertical axis.

Our study being based on field-observed deformation structures, there is also an ambiguity on whether paleostresses represent coseismic (i.e., dynamic) or interseismic (i.e., static) stresses, or even a mixed record of both. Since the main seismic rupture generates most of the deformation, the former interpretation might seem
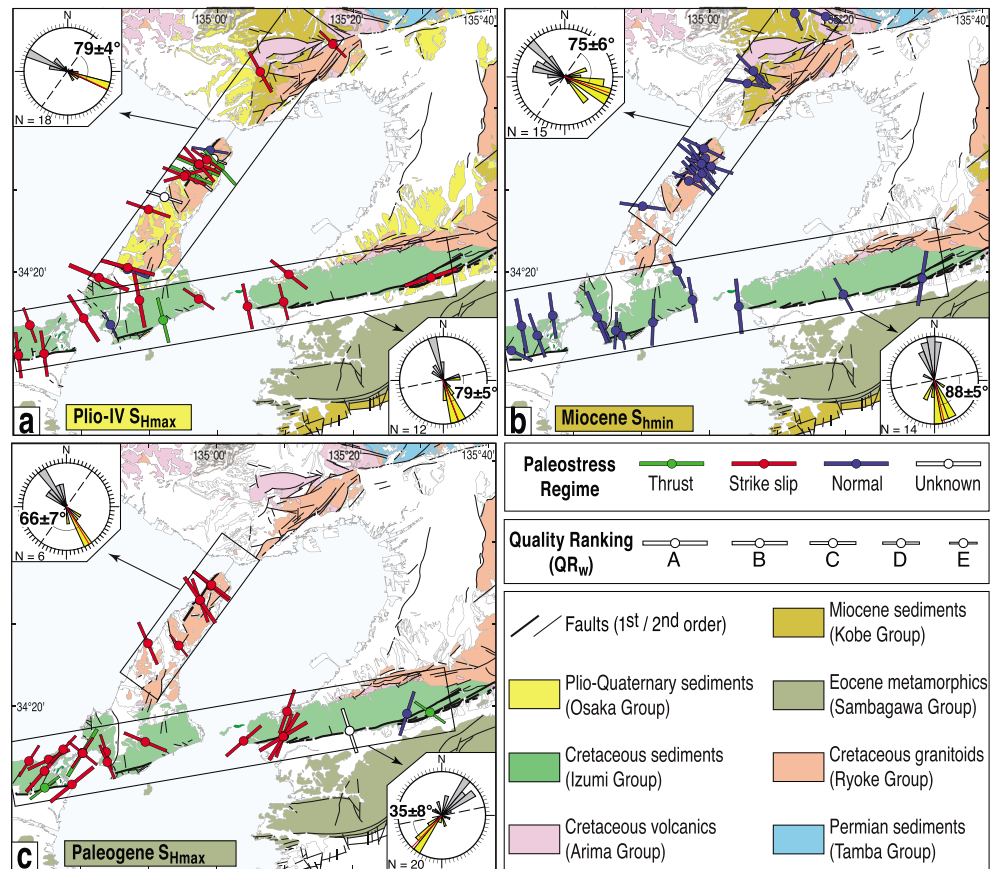
Figure 5. Paleostress orientations deduced from the inversion of fault-slip data. (a) Orientation of the maximum horizontal paleostress (S_{Hmax}) during the Plio-Quaternary. (b) Orientation of the minimum horizontal paleostress (S_{hmin}) during the Miocene. (c) S_{Hmax} during the Paleogene. The quality ranking system comes from the World Stress Map project [*Sperner et al.,* 2003]. Insets are asymmetric rose diagrams of quality-weighted paleostress data, as strikes on the upper, left-hand side of the diagram (in grey), and as angles with fault strands on the lower, right-hand side (in yellow).

appropriate at first glance. However, it is also true that this deformation is essentially accommodated by slip on main faults, rather than on secondary faults sometimes several kilometers away. Our structures are representative of creep (e.g., folds or synkinematic mineral fibers in faults and extension fractures) or of very small seismic ruptures (e.g., < 2 m long faults without gouges) and were thus more likely generated by aseismic deformation or by aftershocks. In addition, there is a good consistency of S_{Hmax} orientations deduced from short-term stress measurements on one side (pre- and post-Kobe earthquake hydraulic fracturing tests and earthquake focal mechanisms; Figure 1), and long-term stress measurements on the other side (microcracks and stress memory in oriented core samples, and paleostresses from this study; Figure 5a) in the immediate vicinity of the Rokko-Awaji Segment. This consistency suggests that paleostresses are comparable to stress orientations measured within interseismic periods. We are thus inclined to interpret paleostresses as static stresses recorded over interseismic periods and perhaps even in postseismic periods (i.e., just after seismic ruptures and in the beginning of interseismic periods).

4.2. Paleostress Rotations

The major result of our study is that paleostress orientations are spatially deviated in the vicinity of the two fault systems during each of the three tectonic periods. In the Plio-Quaternary, paleostress orientations away from the two faults coincide well with the present-day regional stress field inferred from earthquake focal mechanisms (Figures 1 and 5a). However, and despite the optimal orientation of the Median Tectonic Line at 20–40° to the regional E-W direction of maximum compression, S_{Hmax} progressively rotates by 50–70° toward the fault normal, to reach an angle of 79 ± 5° with the fault within a ~5 km wide band (Figure 5a). This band is 5 times wider than the 1 km thickness of gouges, cataclasites, and mylonites estimated by
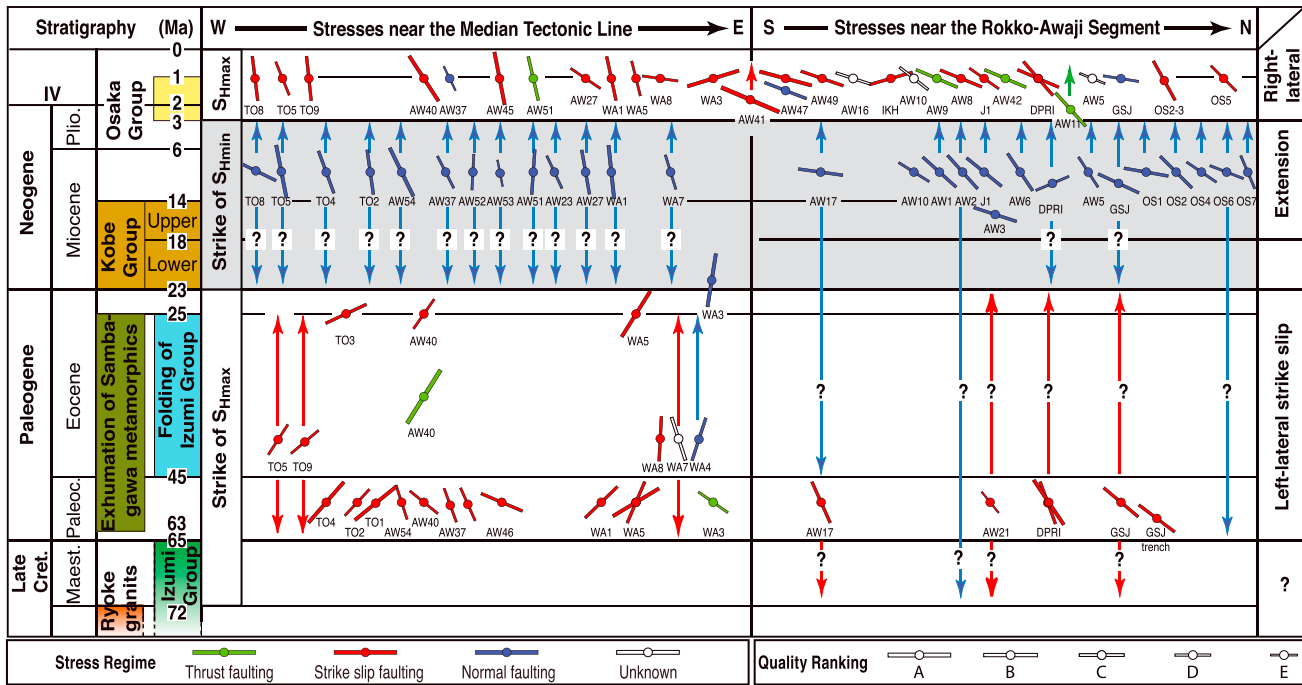
Figure 6. Interpreted chronology of paleostresses. The azimuthal reference is north upward. See Table 2 for paleostress tensor parameters and the supporting information for site locations.

Maruyama and Lin [2004] and may reflect the total width of the Median Tectonic Line including its damaged zone. Likewise, the Rokko-Awaji Segment makes an angle of 45–65° with the E-W regional direction of maximum compression, yet S_{Hmax} rotates by 20–30° to an angle of $79 \pm 4°$ with the fault system, within a band of at least 5 km width. This band of stress rotation is thus wider than the damaged zones of individual faults of the Rokko-Awaji Segment, but similar to the total width of this fault system. During the Miocene, S_{hmin} near the Rokko-Awaji Segment is aligned with the regional NW-SE extension of Japan, yet S_{hmin} rotates by 30–50° near the Median Tectonic Line to become perpendicular to the fault strand (Figure 5b). In the Paleogene, the Rokko-Awaji Segment is almost parallel to the orientation of S_{Hmax} imposed by the Median Tectonic Line, yet appears to locally reorient S_{Hmax} of at least 50° (Figure 5c). Spatial variations of paleostresses have already been documented in the vicinity of crustal faults. For the Highland Boundary Fault Zone (Scotland) at ~60° to the regional compression, *Jones and Tanner* [1995] showed that the maximum shortening direction deduced from fault slip data becomes almost perpendicular to the master fault in its vicinity. Our study suggests that such decoupling remains true even in the extreme case of a fault at low angle with the regional compression like the Median Tectonic Line.

4.3. Possible Causes of Stress Rotations
4.3.1. Low Residual Shear Stress
The interpretation of stress rotations depends on the meaning that we attribute to deformation data and their inversion. If, as discussed above, the structures are considered as strictly postseismic, paleostresses may represent a residual stress state after seismic ruptures. In this case, the rotation of the maximum compressional direction to a high angle with the fault planes has to be interpreted as a relaxation of shear stress by earthquakes. The shear stress drop of earthquakes being generally smaller than 10 MPa [*Scholz*, 2006], this first interpretation implies that the shear stress is variable, yet maintained to a low level throughout the seismic cycle by dynamic weakening. For the most recent rupture of the Rokko-Awaji Segment that occurred on the Nojima fault, seismological and borehole studies concluded on a pre-Kobe earthquake shear stress < 10 MPa and a residual shear stress < 2 MPa on the upper 5 km of crust [*Bouchon et al.*, 1998; *Spudich et al.*, 1998]. Our work suggests that this low level of shear stress before and after earthquakes stands as a general long-term rule since at least the Plio-Quaternary.
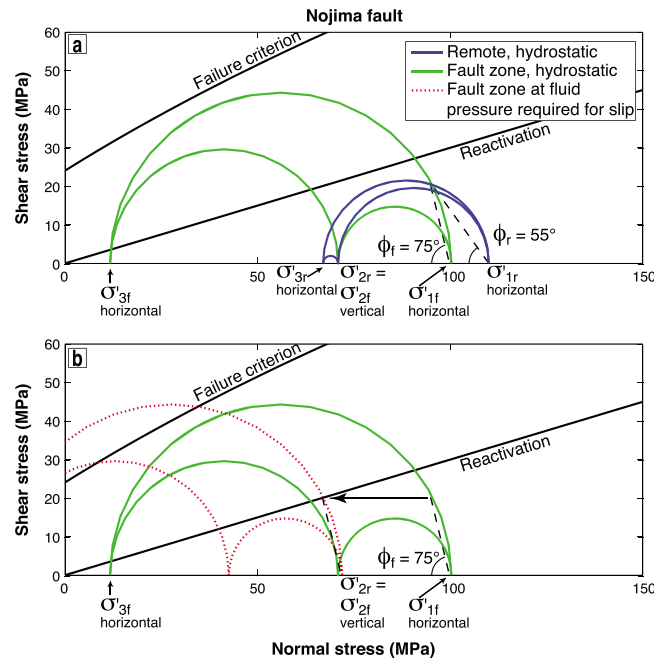
Figure 7. Mohr diagrams illustrating the effect of a rotation of σ_1 toward the fault perpendicular, on the example of the Nojima fault. (a) The blue Mohr circles correspond to a remote effective stress state (denoted by the subscript "r") at 4 km depth at hydrostatic fluid pressure ($\sigma'_1 = S_{Hmax} = 110$ MPa, $\sigma'_2 = \sigma'_v = 71$ MPa, and $\sigma'_3 = S_{hmin} = 67$ MPa, assuming a rock volumetric weight of 27.5 kN/m^3), with the direction of compression at 55° of the fault. The green Mohr circles correspond to a fault zone effective stress state at hydrostatic fluid pressure (denoted by the subscript "f"), drawn by construction with the assumption of 1-D shear and normal stress conservation in the fault normal direction, a constant vertical stress, and a direction of compression at 75° to the fault (the minimum angle for Nojima). (b) The red dashed Mohr circles correspond to the same stress state as the green Mohr circles but at the suprahydrostatic fluid pressure required for activating the Nojima fault. Black lines represent schematic failure criteria of intact rock for shear fracture (Hoek-Brown criterion with $\sigma_{ci} = 230$ MPa, $m_i = 10$, GSI = 40, and D = 0 [*Hoek et al.*, 2002]) and frictional sliding ($\mu = 0.6$, C = 0 MPa [*Byerlee,* 1978]).

4.3.2. Low Static Fault Friction

If paleostresses are rather interpreted as relevant of entire interseismic periods, stress rotations must arise from modifications of the mechanical properties of the fault zone compared with the country rocks. The most obvious possibility for such modification is a low static friction coefficient on the fault relative to intact rock, which causes a reorientation of σ_1 toward the fault-normal direction, and a concentration of shear stress on asperities and at the tips of the fault. Using 2-D modeling of a fault within an isotropic elastic medium, *Homberg et al.* [1997] found that 20–50° rotations of σ_1 toward the fault normal, such as obtained in this study, are achieved on the condition that $\mu < 0.12$. To compare our study with *Homberg et al.* [1997], we computed the average static friction coefficient of the two faults (Appendix A) using the three-dimensional method of fault reactivation analysis by *Leclère and Fabbri* [2013]. This requires knowledge of fault slip vectors, which are only available for the Plio-Quaternary on the Median Tectonic Line and on the Nojima fault. With those slip vectors, the high angle of S_{Hmax} imposes $\mu \leq 0.09$ along the Median Tectonic Line and $\mu \leq 0.15$ along the Nojima fault (Appendix A). Regarding the Nojima fault, our results are in striking agreement with the long-term friction coefficient ($\mu \leq 0.15$)

calculated by *Yamamoto et al.* [2002] from a compilation of stress memory analyses in core samples from three boreholes in the vicinity of the Rokko-Awaji Segment.

4.3.3. Low Elastic Properties

Alternatively, interseismic stress rotations may be interpreted using some 1-D models designed to explain how the San Andreas fault and low-angle normal faults could slip despite being nearly perpendicular to the remote maximum principal stress. These theoretical models propose that σ_1 rotates to a lower angle, more favorable for slip, in the damaged zone or in the core zone of a fault, due to the changing mechanical properties of deformed rocks. In this category, *Casey* [1980] first showed that changes in elastic properties of rocks toward a fault produce changes in stress and strain, compared to the applied stress, which can lead to rotations of σ_1. Then, *Rice* [1992] suggested that a reduction of the differential stress due to the plasticity of the fault zone could be responsible for such rotation. More recently, the elastic theory has been used to propose a rotation of σ_1 toward the fault plane, and a reduction of the differential stress, in response to an elevated Poisson's ratio in fault rocks [*Faulkner et al.,* 2006], or to the combined effects of a fault parallel crack fabric and an elevated pore fluid pressure in the core zone [*Healy,* 2008, 2009]. The most recent category of models is that of *Lecomte et al.* [2011, 2012], in which the rotation of σ_1 to more acute angles is achieved by elastoplastic deformation of the fault zone. All these models are built on the same assumption of shear stress, normal stress, and strain conservation in one
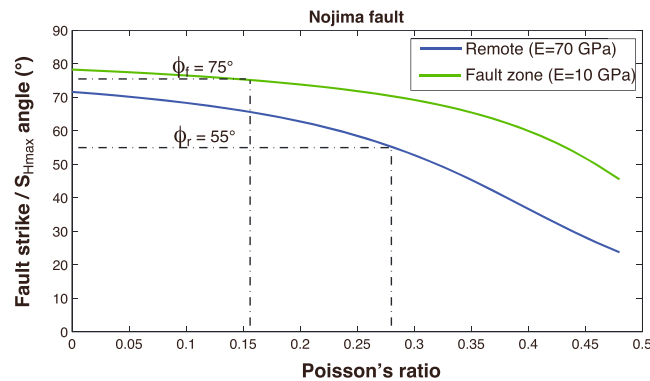
Figure 8. Rotation of the direction of maximum compression with changing elastic properties of fault rocks, according to the 1-D isotropic model of *Faulkner et al.* [2006]. The angle between the fault and S_{Hmax} is drawn as a function of v for E values of 70 GPa (in blue) and 10 GPa (in green). Applied to the Nojima fault, the evolution from intact rock ($E = 70$ GPa; $v = 0.28$) to a heavily fractured and altered fault zone ($E \leq 10$ GPa; $v \leq 0.16$) yields a more fault-normal rotation of S_{Hmax} from 55° to ≥ 75° toward the fault.

dimension along the direction perpendicular to the fault plane. The rotation of σ_1 toward low angles remains a conceptual idea, and its confirmation by stress orientation measurements is still a subject of controversy [*Hardebeck and Hauksson*, 1999, 2001; *Hardebeck and Michael*, 2004; *Provost and Huston*, 2003; *Townend and Zoback*, 2004].

This conceptual idea does not hold in the case of the Median Tectonic Line and the Rokko-Awaji Segment, as the rotation of σ_1 obtained with Plio-Quaternary paleostresses is in the opposite sense. With the assumption of shear and normal stress conservation, such rotation imposes variations of fault zone mechanical properties in opposition with those predicted by the above 1-D models. This is illustrated in Figure 7 for the Nojima fault, again because it is the fault of the Rokko-Awaji Segment for which we have the most precise dip and dip direction constraints. The remote effective stress state is chosen to keep the fault inactivated (as it is before an earthquake) while respecting the ratio $R = 0.09$ of the Quaternary regional stress field [*Tsutsumi et al.*, 2012]. The rotation of stress from the far field (σ_1 at 55° of the fault) to the fault zone (σ_1 at 75°, the minimum angle for the Plio-Quaternary) leads to a reduction of the magnitudes of σ_1 and σ_3 while increasing the differential stress and R (Figure 7a). With a maximum compressional direction at high angle to the fault plane, the stress state before an earthquake is thus closer to shear failure and frictional sliding in the core zone than in the country rock, even in the absence of a greater-than-hydrostatic pore fluid pressure. It is interesting to note that neoformed secondary faults cutting pseudotachylites are found in the core of the Nojima fault (see the GSJ trench site in supporting information but also Figure 5e in *Ohtani et al.* [2000], and Figure 2 in *Boullier et al.* [2001]), providing evidence that the shear failure envelope of rock was reached by the Mohr circle in its core zone.

The observed stress rotation and the related change of stress state cannot be reconciled with plastic or elastoplastic models of fault zone [*Lecomte et al.*, 2011, 2012; *Rice*, 1992]. They can, however, be reconciled with elastic models provided that a marked reduction of both the Young's modulus E and the Poisson's ratio v occurs toward the core zone. This is illustrated in Figure 8, using the isotropically elastic fault zone model of *Faulkner et al.* [2006], for which the rotation of σ_1 from 55° in intact rock to 75° in the fault zone (as for the Nojima fault in the Plio-Quaternary) requires $E \leq 10$ GPa and $v \leq 0.16$. Such low values of E and v could be the consequence of an increasing density of cracks randomly oriented or at high angle with the fault plane [*Healy*, 2008, Figures 4, 6, and 7], but could also be achieved by the alteration of fault rocks into a clay-rich gouge, assuming that clays have low elastic constants that decrease with increasing temperature as do shales [*Alber and Kahraman*, 2009; *Eseme et al.*, 2007].

4.4. Implication for High Pore Fluid Pressures in Fault Zones

Perhaps the most interesting aspect of paleostress rotations is their consequence on the scenario of fault rupture by the buildup of a fluid overpressure. An increasing pore pressure can only trigger fault reactivation without pushing σ_3 into traction if the maximum compressional direction makes an angle ≤ 60° with the fault [*Sibson*, 1985]. The large angle of S_{Hmax} relative to the Median Tectonic Line and the Rokko-Awaji Segment in their vicinity, and even in the core zone of the Nojima fault, imposes the fluid pressure necessary for frictional sliding to be greater than σ_3 (for an initial friction in the range of Byerlee's law). This stress state is prone to lead to failure and the loss of fluid pressure before fault reactivation. The situation is exacerbated under the assumption of shear and normal stresses conservation. It is apparent from Figure 7b that any excess fluid pressure in the Nojima fault zone would push the stress state

furthertoward shear or tensile failure, with the effect of releasing the pressure before activating the fault. Thus, fault rocks do not seem able to sustain the increased fluid pressures necessary to reactivate the Median Tectonic Line or any fault of the Rokko-Awaji Segment under the orientation of paleostresses obtained for the Plio-Quaternary. This, of course, does not preclude the transient existence of pore fluid pressurization during slip.

Dynamic weakening processes have been proposed to occur in the Median Tectonic Line [*Wibberley and Shimamoto*, 2005] and on the Nojima fault [*Famin et al.,* 2008; *Otsuki et al.,* 2003]. Low-friction phyllosilicates have also been reported on the Median Tectonic Line [*Jefferies et al.,* 2006] and to a lesser extent at Nojima [*Tanaka et al.,* 2001]. Thus, dynamic weakening or materials with low frictional/elastic properties are plausible causes of the observed rotation of paleostresses. On the other hand, drilling programs have not found static fluid overpressures at Nojima and are still looking for them on the San Andreas fault [*Wang*, 2011]. Our study suggests that dynamic weakening or materials with low frictional/elastic properties are more plausible causes of fault weakness than are preearthquake elevated pore pressures.

5. Conclusion

From the field study of rock deformation structures, the history of slip on the Median Tectonic Line and the Rokko-Awaji Segment may be divided into a left lateral movement in the Paleogene, a dip slip extensional movement during the Miocene (already documented for the Median Tectonic Line but previously unknown on the Rokko-Awaji Segment), and a right lateral movement during the Plio-Quaternary. The paleostress inversion of deformation structures reveals that the principal horizontal stresses have been rotated by up to 50° in the vicinity of the two fault systems during each of the three tectonic regimes. During the Plio-Quaternary, these rotations resulted in a more fault-normal orientation of the maximum compression to an angle ~79° relative to the fault strands. Nearly fault-normal compression is found in the damaged zones of the two fault systems, and even in the core zone of the Nojima fault, the most famous fault of the Rokko-Awaji Segment. Such stress rotations seem to be generalized in space, along strike of the two fault systems, and in time, over at least the Plio-Quaternary. The high angle of the maximum compression with the faults may be explained by dynamic weakening, low-friction and/or low elastic properties of the fault zones but are not compatible with the buildup of fluid overpressures before an earthquake. The Median Tectonic Line and the Rokko-Awaji Segment are mature strike-slip fault systems cutting granitic rocks, as are the San Andreas fault in California, the Alpine fault in New Zealand, and the Caleta-Caloso fault in Chile. Should their damaged zones and core zones be mechanically comparable, our study suggests that stresses do not rotate favorably in them to allow fault activation by fluid overpressure and that fault weakness rather resides in weak materials or dynamic mechanisms.

Appendix A: Determination of Static Fault Friction

To estimate the static friction coefficient of faults, we adapted the three-dimensional method of fault reactivation analysis of *Leclère and Fabbri* [2013]. The conventions used are summarized in Figure A1. We considered the most general case where the fault plane contains none of the principal stresses. The reference frame (x_1, x_2, and x_3) was chosen to coincide with the directions of σ_1, σ_2, σ_3 so that the stress tensor $\underline{\sigma}$ can be written:

$$\underline{\sigma} = \begin{vmatrix} \sigma_1 & 0 & 0 \\ 0 & \sigma_2 & 0 \\ 0 & 0 & \sigma_3 \end{vmatrix} \tag{A1}$$

Hereafter, the shear stress and the fault normal stress, which depend on five of the six unknowns in $\underline{\sigma}$, are established for a strike-slip fault (i.e., σ_2 vertical) dipping at an angle β, and making an angle θ with σ_1 (Figure A1). Our model may be adapted to thrusts and normal faults simply by permuting the principal stresses.
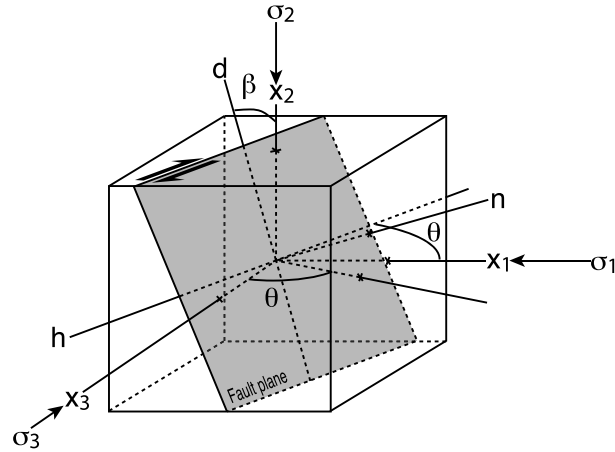
Figure A1. Forces applied to a strike-slip fault plane in three dimensions and conventions used for the computation. The coordinates (x_1, x_2, and x_3) are chosen to coincide with the principal stresses ($\sigma_1 > \sigma_2 > \sigma_3$). The parameter β is the angle of the fault plane relative to the vertical (i.e., 90° fault dip). The parameter θ is the angle between σ_1 and the horizontal in the fault plane. The parameter $\underline{n}$ is a unit vector normal to the fault plane. The parameters $\underline{d}$ and $\underline{h}$ are unit vectors in the dip direction and in the horizontal of the fault plane, respectively.

The normal to the fault plane $\underline{n}$, the horizontal in the plane $\underline{h}$, and the dip direction $\underline{d}$ are unit vectors defined as

$$\underline{n} = \begin{vmatrix} \cos\beta\,\sin\theta \\ \sin\beta \\ \cos\beta\,\cos\theta \end{vmatrix}, \quad \underline{h}$$

$$= \begin{vmatrix} \cos\theta \\ 0 \\ -\sin\theta \end{vmatrix} \text{ and } \underline{d}$$

$$= \begin{vmatrix} \sin\beta\,\sin\theta \\ -\cos\beta \\ \sin\beta\,\cos\theta \end{vmatrix} \tag{A2}$$

The stress vector acting $\underline{F}$ on the fault plane is written as

$$\underline{F} = \underline{\underline{\sigma}} \cdot \underline{n} = \begin{vmatrix} \sigma_1\,\cos\beta\,\sin\theta \\ \sigma_2\,\sin\beta \\ \sigma_3\,\cos\beta\,\cos\theta \end{vmatrix} \tag{A3}$$

$\underline{F}$ may be decomposed as a stress normal to the fault plane (σ), plus two stresses parallel to the fault plane in the horizontal direction (τ_h) and in the dip direction (τ_d):

$$\sigma = \underline{F} \cdot \underline{n}, \quad \tau_h = \underline{F} \cdot \underline{h} \text{ and } \tau_d = \underline{F} \cdot \underline{d} \tag{A4}$$

The shear stress is

$$\tau = \sqrt{\tau_h^2 + \tau_d^2} \tag{A5}$$

Substituting equations (A2) and (A3) into (A4) and (A5) yields

$$\begin{cases} \sigma = \sigma_1\,\cos^2\beta\,\sin^2\theta + \sigma_2\,\sin^2\beta + \sigma_3\,\cos^2\beta\,\cos^2\theta \\ \tau = \sqrt{\cos^2\beta\,\cos^2\theta\,\sin^2\theta(\sigma_1 - \sigma_3)^2 + \cos^2\beta\,\sin^2\beta(\sigma_1\,\sin^2\theta - \sigma_2 + \sigma_3\,\cos^2\theta)^2} \end{cases} \tag{A6}$$

Total stresses are converted into effective stresses by subtracting the fluid pressure P:

$$\sigma'_1 = (\sigma_1 - P), \quad \sigma'_2 = (\sigma_2 - P); \quad \sigma'_3 = (\sigma_3 - P); \quad \sigma' = (\sigma - P) \tag{A7}$$

We assume that the maximum resolved shear stress on the fault plane is collinear with the slip vector α, computed as the ratio of dip slip (taken positive for thrusting) and horizontal slip [*Angelier*, 1990]:

$$\tau_d = \alpha\tau_h \tag{A8}$$

Substituting equation (A8) into (A5), (A6), (A7) yields

$$\sigma'_2 = \sigma'_1\,\sin^2\theta + \sigma'_3\,\cos^2\theta - \frac{\alpha\,\cos\theta\,\sin\theta}{\sin\beta}(\sigma'_1 - \sigma'_3) \tag{A9}$$

Defining $r' = \sigma'_1/\sigma'_3$ and substituting equations (A7) and (A9) into (A6), the ratio of shear stress over normal stress (T_s) may be expressed as

$$T_s = \frac{\sqrt{(1 + \alpha^2)\cos^2\beta\,\cos^2\theta\,\sin^2\theta(r' - 1)^2}}{\sin^2\theta(r' - 1) - \alpha\,\sin\beta\,\cos\theta\,\sin\theta(r' - 1) + 1} \tag{A10}$$

During the Plio-Quaternary, α was equal to ~0.1 on average on the Median Tectonic Line (0.9–6 mm/yr in horizontal and 0.1–0.6 mm/yr in vertical; [*Tsutsumi and Okada*, 1996]) and ~0.5 on the Nojima fault

(0.9–1.0 mm/yr in horizontal and 0.4–0.45 mm/yr in vertical; [*Murata et al.,* 2001]). We assumed that the present-day dips (β) of the Median Tectonic Line (30–40°N [*Ito et al.,* 1996]) and the Nojima fault (83°SE [*Murata et al.,* 2001]) have remained constant over the Plio-Quaternary. For the ratio r', an upper bound of 4.7 is imposed by the Mohr failure envelop of intact rocks according to Byerlee's law. The angle θ, given by our microtectonic study, is of 79° for both faults.

References

Alber, M., and S. Kahraman (2009), Predicting the uniaxial compressive strength and elastic modulus of a fault breccia from texture coefficient, *Rock Mech. Rock Eng.*, *42*(1), 117–127.

Angelier, J. (1984), Tectonic analysis of fault slip data sets, *J. Geophys. Res.*, *89*, 5835–5848, doi:10.1029/JB089iB07p05835.

Angelier, J. (1990), Inversion of field data in fault tectonics to obtain the regional stress. 3. A rapid direct inversion method by analytical means, *Geophys. J. Int.*, *103*(2), 363–376.

Balfour, N. J., M. K. Savage, and J. Townend (2005), Stress and crustal anisotropy in Marlborough, New Zealand: Evidence for low fault strength and structure-controlled anisotropy, *Geophys. J. Int.*, *163*(3), 1073–1086.

Boness, N. L., and M. D. Zoback (2006), Mapping stress and structurally controlled crustal shear velocity anisotropy in California, *Geology*, *34*(10), 825.

Bott, M. H. P. (1959), The mechanisms of oblique slip faulting, *Geol. Mag.*, *96*, 109–117.

Bouchon, M., H. Sekiguchi, K. Irikura, and T. Iwata (1998), Some characteristics of the stress field of the 1995 Hyogo-ken Nanbu (Kobe) earthquake, *J. Geophys. Res.*, *103*, 24,271–24,282, doi:10.1029/98JB02136.

Boullier, A. M., T. Ohtani, K. Fujimoto, and H. Ito (2001), Fluid inclusions in pseudotachylites from the Nojima fault, Japan, *J. Geophys. Res.*, *106*, 21,965–21,977, doi:10.1029/2000JB000043.

Boullier, A. M., K. Fujimoto, H. Ito, T. Ohtani, N. Keulen, O. Fabbri, D. Amitrano, M. Dubois, and P. Pezard (2004), Structural evolution of the Nojima fault (Awaji Island, Japan) revisited from the GSJ drill hole at Hirabayashi, *Earth Planets Space*, *56*, 1233–1240.

Byerlee, J. (1978), Friction of rocks, *Pure Appl. Geophys.*, *116*, 615–627.

Casey, M. (1980), Mechanics of shear zones in isotropic dilatant materials, *J. Struct. Geol.*, *2*(1–2), 143–147.

Delvaux, D. (2013), Version 4.04 and above of the Win-Tensor Program. [Available at http://users.skynet.be/damien.delvaux/Tensor/tensor-index.html.]

Delvaux, D., and B. Sperner (2003), New aspects of tectonic stress inversion with reference to the TENSOR program, in *New Insights Into Structural Interpretation and Modelling*, edited by D. A. Nieuwland, *Geol. Soc. London Spec. Publ.*, *212*, 75–100.

Delvaux, D., F. Kervyn, A. S. Macheyeki, and E. B. Temu (2012), Geodynamic significance of the TRM segment in the East African Rift (W-Tanzania): Active tectonics and paleostress in the Ufipa plateau and Rukwa basin, *J. Struct. Geol.*, *37*, 161–180.

Di Toro, G., D. L. Goldsby, and T. E. Tullis (2004), Friction falls towards zero in quartz rock as slip velocity approaches seismic rates, *Nature*, *427*, 436–439.

Dziewonski, A., G. Ekstrom, and M. Salganik (1996), Centroid-moment tensor solutions for January–March 1995, *Phys. Earth Planet. Inter.*, *93*, 147–157.

Eseme, E., J. L. Urai, B. M. Krooss, and R. Littke (2007), Review of mechanical properties of oil shales: Implications for exploitation and basin modelling, *Oil Shale*, *24*(2), 150–174.

Famin, V., S. Nakashima, A.-M. Boullier, K. Fujimoto, and T. Hirono (2008), Earthquakes produce carbon dioxide in crustal faults, *Earth Planet. Sci. Lett.*, *265*(3–4), 487–497.

Faulkner, D. R., T. M. Mitchell, D. Healy, and M. J. Heap (2006), Slip on 'weak' faults by the rotation of regional stress in the fracture damage zone, *Nature*, *444*(7121), 922–925.

Fournier, M., L. Jolivet, and O. Fabbri (1995), Neogene stress field in SW Japan and mechanism of deformation during the Sea of Japan opening, *J. Geophys. Res.*, *100*, 24,295–24,314, doi:10.1029/95JB01973.

Hardebeck, J. L., and E. Hauksson (1999), Role of fluids in faulting inferred from stress field signatures, *Science*, *285*, 236–240.

Hardebeck, J. L., and E. Hauksson (2001), Crustal stress field in southern California and its implications for fault mechanics, *J. Geophys. Res.*, *106*, 21,859–21,882, doi:10.1029/2001JB000292.

Hardebeck, J. L., and A. J. Michael (2004), Stress orientations at intermediate angles to the San Andreas Fault, California, *J. Geophys. Res.*, *109*, B11303, doi:10.1029/2004JB003239.

Hayashida, H., H. Kamata, and T. Danhara (1996), Correlation of widespread tephra deposits based on paleomagnetic directions: Link between a volcanic field and sedimentary sequences in Japan, *Quat. Int.*, *34–36*, 89–98.

Healy, D. (2008), Damage patterns, stress rotations and pore fluid pressures in strike-slip fault zones, *J. Geophys. Res.*, *113*, B12407, doi:10.1029/2008JB005655.

Healy, D. (2009), Anisotropy, pore fluid pressure and low angle normal faults, *J. Struct. Geol.*, *31*(6), 561–574.

Hickman, S., and M. D. Zoback (2004), Stress orientations and magnitudes in the SAFOD pilot hole, *Geophys. Res. Lett.*, *31*, L15S12, doi:10.1029/2004GL020043.

Hoek, E., C. Carranza-Torres, and B. Corkum (2002), Hoek-Brown failure criterion - 2002 Edition, *Rep.*

Homberg, C., J. C. Hu, J. Angelier, F. Bergerat, and O. Lacombe (1997), Characterization of stress perturbations near major fault zones: Insights from 2-D distinct-element numerical modelling and field studies (Jura mountains), *J. Struct. Geol.*, *19*(5), 703–718.

Homberg, C., J. Angelier, F. Bergerat, and O. Lacombe (2004), Using stress deflections to identify slip events in fault systems, *Earth Planet. Sci. Lett.*, *217*(3–4), 409–424.

Hyodo, M., D. K. Biswas, T. Noda, N. Tomioka, T. Mishima, C. Itota, and H. Sato (2006), Millennial- to submillennial-scale features of the Matuyama-Brunhes geomagnetic polarity transition from Osaka Bay, southwestern Japan, *J. Geophys. Res.*, *111*, B02103, doi:10.1029/2004JB003584.

Igi, S., and C. Chosajo (1981), 1:200,000 geological map of Himeji, NI-53-20, Geol. Surv. of Jpn.

Ikeda, M., S. Kato, N. Nishizaka, Y. Ohno, K. Matsuo, and M. Kishimoto (2013), Magnetotelluric imaging of the Median Tectonic Line in western Shikoku, southwest Japan: Implications of the fault-related low-resistivity zone, *Tectonophysics*, *601*, 78–86.

Ikeda, R., Y. Iio, and K. Omura (2001), In situ stress measurements in NIED boreholes in and around the fault zone near the 1995 Hyogo-ken Nanbu earthquake, Japan, *Isl. Arc*, *10*(3–4), 252–260.

Ito, H., and T. Kiguchi (2005), Distribution and properties of fractures in and around the Nojima Fault in the Hirabayashi GSJ borehole, in *Petrophysical Properties of Crystalline Rocks*, edited by P. K. Harvey et al., *Geol. Soc. London Spec. Publ.*, *240*, 61–74.

Ito, T., T. Ikawa, S. Yamakita, and K. Maeda (1996), Gently north-dipping Median Tectonic Line (MTL) revealed by recent seismic reflection studies, southwest Japan, *Tectonophysics*, *1996*, 51–63.

Iwaki, H., and A. Hayashida (2003), Paleomagnetism of Pleistocene widespread tephra deposits and its implication for tectonic rotation in central Japan, *Isl. Arc*, *12*(1), 46–60.

Jefferies, S. P., R. E. Holdsworth, T. Shimamoto, H. Takagi, G. E. Lloyd, and C. J. Spiers (2006), Origin and mechanical significance of foliated cataclastic rocks in the cores of crustal-scale faults: Examples from the Median Tectonic Line, Japan, *J. Geophys. Res.*, *111*, B12303, doi:10.1029/2005JB004205.

Jones, R. R., and P. W. G. Tanner (1995), Strain partitioning in transpression zones, *J. Struct. Geol.*, *17*(6), 793–802.

Kawada, K., M. Miyamura, and F. Yoshida (1986), 1:200,000 map of Kyoto-Osaka, NI-53-14, Geol. Surv. of Jpn.

Kipata, M. L., D. Delvaux, M. Sebagenzi, J. Cailteux, and M. Sintubin (2013), Brittle tectonic and stress field evolution in the Pan-African Lufilian arc and its foreland (Katanga, DRC): From orogenic compression to extensional collapse, transpressional inversion and transition to rifting, *Geol. Belg.*, *16*(1–2), 1–17.

Kodama, K. (1986), Two different paleomagnetic directions from the Izumi Group in Shikoku, Southwest Japan, *J. Geomagn. Geoelectr.*, *38*(4), 279–284.

Kodama, K. (1989), Paleomagnetic study of the upper Cretaceous Izumi strike-slip basin along the Median Tectonic Line in southwest Japan, in *Deep Structure and Past Kinematics of Accreted Terranes*, edited by J. W. Hillhouse, pp. 239–248, AGU, Washington, D. C.

Kubota, Y., and T. Takeshita (2008), Paleocene large-scale normal faulting along the Median Tectonic Line, western Shikoku, Japan, *Isl. Arc*, *17*(1), 129–151.

Kurimoto, C., and M. Komazawa (1998), 1:200,000 map of Wakayama, NI-53-15, Geol. Surv. of Jpn.

Lacombe, O. (2012), Do fault slip data inversions actually yield "paleostresses" that can be compared with contemporary stresses? A critical discussion, *C. R. Geosci.*, *344*(3–4), 159–173.

Leclère, H., and O. Fabbri (2013), A new three-dimensional method of fault reactivation analysis, *J. Struct. Geol.*, *48*, 153–161.

Lecomte, E., L. Le Pourhiet, O. Lacombe, and L. Jolivet (2011), A continuum mechanics approach to quantify brittle strain on weak faults: Application to the extensional reactivation of shallow dipping discontinuities, *Geophys. J. Int.*, *184*(1), 1–11.

Lecomte, E., L. Le Pourhiet, and O. Lacombe (2012), Mechanical basis for slip along low-angle normal faults, *Geophys. Res. Lett.*, *39*, L03307, doi:10.1029/2011GL050756.

Lin, A. M. (2001), S-C fabrics developed in cataclastic rocks from the Nojima fault zone, Japan and their implications for tectonic history, *J. Struct. Geol.*, *23*(6–7), 1167–1178.

Lin, A. M., T. Shimamoto, T. Maruyama, M. Sigetomi, T. Miyata, K. Takemura, H. Tanaka, S. Uda, and A. Murata (2001), Comparative study of cataclastic rocks from a drill core and outcrops of the Nojima Fault zone on Awaji Island, Japan, *Isl. Arc*, *10*(3–4), 368–380.

Lockner, D. A., H. Tanaka, H. Ito, R. Ikeda, K. Omura, and H. Naka (2009), Geometry of the Nojima fault at Nojima-Hirabayashi, Japan—I. A simple damage structure inferred from borehole core permeability, *Pure Appl. Geophys.*, *166*(10–11), 1649–1667.

Lockner, D. A., C. Morrow, D. Moore, and S. Hickman (2011), Low strength of deep San Andreas fault gouge from SAFOD core, *Nature*, *472*(7341), 82–85.

Lund, B., and J. Townend (2007), Calculating horizontal stress orientations with full or partial knowledge of the tectonic stress tensor, *Geophys. J. Int.*, *170*(3), 1328–1335.

Maenaka, K. (1979), Paleomagnetic study of sediments around the Komyoke volcanic ash horizon, *Geophys. Res. Lett.*, *6*, 257–260, doi:10.1029/GL006i004p00257.

Makimoto, H., M. Komazawa, and R. Shichi (1995), 1:200,000 map of Tokushima, NI-53-21.

Maruyama, T., and A. M. Lin (2004), Slip sense inversion on active strike-slip faults in southwest Japan and its implications for Cenozoic tectonic evolution, *Tectonophysics*, *383*(1–2), 45–70.

Miller, D. (1998), Distributed shear, rotation, and partitioned strain along the San Andreas fault, central California, *Geology*, *26*(10), 867–870.

Miyata, T. (1990), Slump strain indicative of paleoslope in Cretaceous Izumi sedimentary basin along Median tectonic line, southwest Japan, *Geology*, *18*(5), 392–394.

Mizuno, T., and K. Nishigami (2006), Deep structure of the Nojima Fault, southwest Japan, estimated from borehole observations of fault-zone trapped waves, *Tectonophysics*, *417*(3–4), 231–247.

Mizuno, T., Y. Kuwahara, H. Ito, and K. Nishigami (2008), Spatial variations in fault-zone structure along the Nojima fault, Central Japan, as inferred from borehole observations of fault-zone trapped waves, *Bull. Seismol. Soc. Am.*, *98*(2), 558–570.

Mount, V. S., and J. Suppe (1987), State of stress near the San Andreas fault: Implications for wrench tectonics, *Geology*, *15*(12), 1143–1146.

Murakami, M., and T. Tagami (2004), Dating pseudotachylyte of the Nojima fault using the zircon fission-track method, *Geophys. Res. Lett.*, *31*, L12604, doi:10.1029/2004GL020211.

Murata, A., K. Takemura, T. Miyata, and A. Lin (2001), Quaternary vertical offset and average slip rate of the Nojima Fault on Awaji Island, Japan, *Isl. Arc*, *10*(3–4), 360–367.

Ohtani, T., K. Fujimoto, H. Ito, H. Tanaka, N. Tomida, and T. Higuchi (2000), Fault rocks and past to recent fluid characteristics from the borehole survey of the Nojima fault ruptured in the 1995 Kobe earthquake, southwest Japan, *J. Geophys. Res.*, *106*, 16,161–16,171, doi:10.1029/2000JB900086.

Ohtani, T., H. Tanaka, K. Fujimoto, T. Higuchi, N. Tomida, and H. Ito (2001), Internal structure of the Nojima Fault zone from the Hirabayashi GSJ drill core, *Isl. Arc*, *10*(3–4), 392–400.

Otofuji, Y., and T. Matsuda (1996), Large tectonic movement of the Japan arc in late Cenozoic times inferred from paleomagnetism; Review and synthesis, *Isl. Arc*, *5*, 229–240.

Otsuki, K., N. Monzawa, and T. Nagase (2003), Fluidization and melting of fault gouge during seismic slip: Identification in the Nojima fault zone and implications for focal earthquake mechanisms, *J. Geophys. Res.*, *108*(B4), 2192, doi:10.1029/2001JB001711.

Provost, A.-S., and H. Huston (2003), Stress orientation in north and central California: Evidence for the evolution of frictional strength along the San Andreas plate boundary system, *J. Geophys. Res.*, *108*(B3), 2175, doi:10.1029/2001JB001123.

Rice, J. (1992), Fault stress states, pore pressure distributions, and the weakness of San Andreas fault, in *Fault Stress States, Pore Pressure Distributions, and Transport Properties of Rocks: A Festschrift in Honor of W. F. Brace*, edited by B. Evans and T. F. Wong, pp. 475–503, Calif. Acad. Press, San Diego, Calif.

Scholz, C. H. (2006), The strength of the San Andreas fault: A critical analysis, in *Earthquakes: Radiated Energy and the Physics of Faulting*, edited by R. Abercrombie et al., pp. 301–311, AGU, Washington, D. C.

Sibson, R. H. (1985), A note on fault reactivation, *J. Struct. Geol.*, *7*, 751–754.

Sperner, B., and P. Zweigel (2010), A plea for more caution in fault-slip analysis, *Tectonophysics*, *482*(1–4), 29–41.

FAMIN ET AL.   1918

Sperner, B., B. Müller, O. Heidbach, D. Delvaux, J. Reinecker, and K. Fuchs (2003), Tectonic stress in the Earth's crust: Advances in the World Stress Map project, in *New Insights Into Structural Interpretation and Modelling*, edited by D. A. Nieuwland, *Geol. Soc. London Spec. Publ.*, *212*, 101–116.

Spudich, P., M. Guatteri, K. Otsuki, and J. Minagawa (1998), Use of fault striations and dislocation models to infer tectonic shear stress during the 1995 Hyogo-ken Nanbu (Kobe) earthquake, *Bull. Seismol. Soc. Am.*, *88*(2), 413–427.

Tabei, T., M. Adachi, S. Miyazaki, T. Watanabe, and S. Kato (2007), Interseismic deformation of the Nankai subduction zone, southwest Japan, inferred from three-dimensional crustal velocity fields, *Earth Planets Space*, *59*(10), 1073–1082.

Takagi, H. (1986), Implications of mylonitic microstructures for the geotectonic evolution of the Median Tectonic Line, Central Japan, *J. Struct. Geol.*, *8*(1), 3–14.

Takeshita, T., and K. Yagi (2001), Paleostress orientation from 3-D orientation distribution of microcracks in quartz from the Cretaceous granodiorite core samples drilled through the Nojima Fault, south-west Japan, *Isl. Arc*, *10*(3–4), 495–505.

Tanaka, H., K. Fujimoto, T. Ohtani, and H. Ito (2001), Structural and chemical characterization of shear zones in the freshly activated Nojima fault, Awaji Island, southwest Japan, *J. Geophys. Res.*, *106*, 8789–8810, doi:10.1029/2000JB900444.

Tanaka, H., K. Omura, T. Matsuda, R. Ikeda, K. Kobayashi, M. Murakami, and K. Shimada (2007), Architectural evolution of the Nojima fault and identification of the activated slip layer by Kobe earthquake, *J. Geophys. Res.*, *112*, B07304, doi:10.1029/2005JB003977.

Tavarnelli, E., and R. E. Holdsworth (1999), How long do structures take to form in transpression zones? A cautionary tale from California, *Geology*, *27*(12), 1063–1066.

Tembe, S., D. Lockner, and T.-f. Wong (2009), Constraints on the stress state of the San Andreas Fault with analysis based on core and cuttings from San Andreas Fault Observatory at Depth (SAFOD) drilling phases 1 and 2, *J. Geophys. Res.*, *114*, B11401, doi:10.1029/2008JB005883.

Townend, J., and M. D. Zoback (2001), Implications of earthquake focal mechanisms for the frictional strength of the San Andreas fault system, *Geol. Soc. London Spec. Publ.*, *186*(1), 13–21.

Townend, J., and M. D. Zoback (2004), Regional tectonic stress near the San Andreas fault in central and southern California, *Geophys. Res. Lett.*, *31*, L15S11, doi:10.1029/2003GL018918.

Townend, J., and M. D. Zoback (2006), Stress, strain, and mountain building in central Japan, *J. Geophys. Res.*, *111*, B03411, doi:10.1029/2005JB003759.

Tsutsumi, H., and A. Okada (1996), Segmentation and Holocene surface faulting on the Median Tectonic Line, southwest Japan, *J. Geophys. Res.*, *101*, 5855–5871, doi:10.1029/95JB01913.

Tsutsumi, H., K. Sato, and A. Yamaji (2012), Stability of the regional stress field in central Japan during the late Quaternary inferred from the stress inversion of the active fault data, *Geophys. Res. Lett.*, *39*, L23303, doi:10.1029/2012GL054094.

Twiss, R. J., and J. R. Unruh (1998), Analysis of fault slip inversions: Do they constrain stress or strain rate?, *J. Geophys. Res.*, *103*, 12,205–12,222, doi:10.1029/98JB00612.

Uno, K. (2002), Late Cretaceous paleomagnetic results from Southwest Japan: New insights for early Cenozoic clockwise rotation, *Geophys. J. Int.*, *149*, 617–624.

Wallace, R. E. (1951), Geometry of shearing stress and relation to faulting, *J. Struct. Geol.*, *59*, 118–130.

Wang, C. y. (2011), High pore pressure, or its absence, in the San Andreas Fault, *Geology*, *39*(11), 1047–1050.

Wesson, R. L., and O. S. Boyd (2007), Stress before and after the 2002 Denali fault earthquake, *Geophys. Res. Lett.*, *34*, L07303, doi:10.1029/2007GL029189.

Wibberley, C. A. J., and T. Shimamoto (2005), Earthquake slip weakening and asperities explained by thermal pressurization, *Nature*, *436*(7051), 689–692.

Yamamoto, K., and Y. Yabe (2001), Stresses at sites close to the Nojima Fault measured from core samples, *Isl. Arc*, *10*(3–4), 266–281.

Yamamoto, K., N. Sato, and Y. Yabe (2002), Elastic property of damaged zone inferred from in-situ stresses and its role on the shear strength of faults, *Earth Planets Space*, *54*(11), 1181–1194.

Zhao, S., and S. Takemoto (1998), Aseismic fault movement before the 1995 Kobe earthquake detected by a GPS survey: Implication for preseismic stress localization?, *Geophys. J. Int.*, *135*(2), 595–606.

Zoback, M. D., et al. (1987), New evidence on the state of stress of the San Andreas fault system, *Science*, *238*, 1105–1111.

Zoback, M. D., S. Hickman, and W. Ellsworth (2011), Scientific drilling into the San Andreas Fault Zone— An overview of SAFOD's first five years, *Sci. Drill.*, *11*, 14–28.

Zwingmann, H., K. Yamada, and T. Tagami (2010), Timing of brittle deformation within the Nojima fault zone, Japan, *Chem. Geol.*, *275*(3–4), 176–185.